Mantle Thermochemical Variations beneath the Continental United States Through Petrologic Interpretation of Seismic Tomography

Shinevar William[1], Golos Eva[2], Jagoutz Oliver[3], Behn Mark D[4], and Van Der Hilst Robert D[3]

[1]University of Colorado Boulder
[2]University of Wisconsin-Madison
[3]Massachusetts Institute of Technology
[4]University of Colorado

November 16, 2022

Abstract

The continental lithospheric mantle plays an essential role in stabilizing continents over long geological time scales. Quantifying spatial variations in compositional and thermochemical properties of the mantle lithosphere is crucial to understanding its formation and its impact on continental stability; however, our understanding of these variations remains limited. Here we apply the Whole-rock Interpretive Seismic Toolbox For Ultramafic Lithologies (WISTFUL) to estimate thermal, compositional, and density variations in the continental mantle beneath the contiguous United States from MITPS_20, a joint body and surface wave tomographic inversion for Vp and Vs with high resolution in the shallow mantle (60-100 km). Our analysis shows lateral variations in temperature beneath the continental United States of up to 800–900°C at 60, 80, and 100 km depth. East of the Rocky Mountains, the mantle lithosphere is generally cold (350–850°C at 60 km), with higher temperatures (up to 1000°C at 60 km) along the Atlantic coastal margin. By contrast, the mantle lithosphere west of the Rocky Mountains is hot (typically >1000°C at 60 km, >1200°C at 80–100 km), with the highest temperatures beneath Holocene volcanoes. In agreement with previous work, we find that the predicted chemical depletion does not fully offset the density difference due to temperature. Extending our results using Rayleigh-Taylor instability analysis, implies the lithosphere below the United States could be undergoing oscillatory convection, in which cooling, densification, and sinking of a chemically buoyant layer alternates with reheating and rising of that layer.

Supplemental Information for Mantle Thermochemical Variations beneath the Continental United States Through Petrologic Interpretation of Seismic Tomography

William J. Shinevar[1*], Eva M. Golos[2], Oliver Jagoutz[3], Mark D. Behn[4], Robert Van der Hilst[3]

[1] MIT/WHOI Joint Program in Oceanography/Applied Ocean Engineering

[2] Brown University

[3] Massachusetts Institute of Technology

[4] Boston College

[*]now at University of Colorado Boulder

This supplement contains two supplemental tables containing compiled xenolith and primary magma thermobarometry, two supplemental figures, and a data file containing the results plotted in Figures 3-6.

Supplementary Information:

Comparison with primary magma thermobarometry

Another temperature comparison is with primary magma thermobarometry, which uses compositions of primary magmas and primary melt inclusions to calculate the pressure and temperature at which a melt was last in equilibrium with the mantle (c.f. Till, 2017). Here we use temperatures estimated from different thermometers that incorporate both tholeiitic and alkaline samples (Leeman *et al.* , 2005; Ruscitto *et al.* , 2010; Till *et al.* , 2013; Plank and Forsyth, 2016; Till, 2017). We also include recalculated temperature estimates from high-Mg andesites from Mt. Shasta (Baker et al., 1994; Grove et al., 2002) using the thermometer of Mitchell and Grove (2015) at 1.5 GPa (Mt. Shasta, coldest blue square, Figure S7) (Supplementary Table 2). Due to the importance of measuring H_2O and CO_2 on the liquidus temperature and pressure, we only use estimates made with measured H_2O based on melt inclusions. As volatiles rapidly diffuse from melt inclusions (Bucholz et al., 2013; Gaetani et al., 2012), the temperature estimates for hydrous melting using these water contents are an upper bound (Till, 2017), but generally agree with estimates from regional tholeiitic primary magmas. To compare regions with different numbers of estimates, we bin magmatic temperature estimates into 0.5°x0.5° regions for pressure estimates within 0.3 GPa of the regional pressures at 60 and 80 km. We take the uncertainty in the magmatic temperature estimates to be the maximum of the reported uncertainty or the standard deviation of averaged estimates. This binned temperature estimate is compared with the mean temperature of our results at the relative depths slices within 0.5° arc-distance. Uncertainty in our temperature results is defined as the maximum between the average temperature uncertainty and the standard deviation of averaged temperatures.

Our results underpredict magmatic temperatures estimates (square, Figure S1). On average, we underpredict magmatic temperature estimates beyond estimated uncertainty (RMSE=260°C at 60 km, 110°C at 80 km). There are multiple hypotheses for this disagreement: (1) scale of the temperature estimates, (2) error in the anelastic correction of seismic wave speeds, (3) error in the magmatic thermobarometers, or (4) error in the forward calculation of mantle seismic wave speeds, potentially due to the exclusion of melt or hydrous phases. The following paragraphs discuss these possibilities.

The first potential cause for the systematic difference in our results and magmatic temperature estimates is the scale over which each is measuring. Magmatic temperature estimates sample the temperature at which the melt was in equilibrium with the mantle and may only represent small regions (~1 m) of the mantle, especially if melt is focused (e.g., Kelemen and Dick, 1995) and/or escapes the mantle on short (~10 kyr) timescales (Feineman and DePaolo, 2003). Conversely, seismic tomographic inversions such as MITPS_20 are limited to resolving seismic anomalies greater than ~1.5°x1.5° with vertical resolution on the order of 10 km (Golos et al., 2020). Thus, non-pervasive, small-scale seismic anomalies due to thermal upwellings or melt may be smeared or not sensed. Furthermore, seismic inversions smooth their wave speeds in order to stabilize the inversion, though MITPS_20 corrects for some of this effect (see Methodology). Subduction zones are especially difficult to image due to any smearing of the cold, subducting lithosphere, which increases seismic wave speed, decreasing the temperature estimate. The fact that the 80-km temperatures are in better agreement with magmatic estimates may suggest that at 60 km, vertical smearing may increase the inverted seismic wave speeds as the tomography samples from starkly colder lithosphere along a steep geotherm. Regional, high-resolution seismic studies are necessary to understand these effects.

A second reason for the temperature discrepancy could be error in anelastic corrections of seismic wave speed. Anelasticity experiments on olivine and peridotite are difficult, with various experimental groups giving different results and sensitivities (Faul and Jackson, 2015; Karato and Park, 2018). The Behn *et al.* (2009) power-law formulation of anelasticity does not fit experimental data well at low quality factors (Q^{-1}>0.1, high temperatures or melt present. Jackson and Faul, 2010). Certain parameters in the both anelasticities are relatively unconstrained, like the activation volume that controls the pressure sensitivity (Faul and Jackson, 2015; Jackson and Faul, 2010). Other comparisons of high-quality seismic experiments and forward calculations of peridotite seismic wave speeds required altering the relaxation peak of the frequencies in order for the observations to be interpreted by the Jackson and Faul (2010) anelasticity (Ma et al., 2020). Furthermore, the effect of water content on anelasticity is currently debated (Aizawa et al., 2008; Cline et al., 2018; Karato and Park, 2018). Increasing the water content decreases V_s at high temperatures, thus shifting all forward calculations above ˜900°C to the left in Figure 2. As we assumed relatively dry water contents (C_{OH}=50 H/10^6 Si), assuming an increased water content would decrease the interpreted temperatures. While grain size is an important parameter for anelasticities (Behn et al., 2009; Faul and Jackson, 2005), we have assumed a reasonable grain size near the upper bound observed in xenoliths. Any grain size reduction increases anelastic effects, thus reducing the modeled temperature. Therefore, variable grain size and its effect on anelasticity cannot reconcile the temperature discrepancy discussed here. Oxidation has been found to increase dissipation (Cline et al., 2018), not incorporated in our methods. This would also reduce our temperature results in arc settings as arc mantle is more oxidized (Kelley and Cottrell, 2012). Conversely, as long as melt and fluids are focused, oxidation would not decrease large-scale seismic wave speed as only a small portion of the mantle may be highly oxidized.

While increasing water content can drastically reduce the peridotite solidus, tholeiitic (dry) magmas are observed in the western United States (Till, 2017). Melting experiments on dry peridotite compositions require temperatures >1300°C at 60 km depth, greater than nearly all our temperature results (Hirschmann, 2000). Given the existence of Holocene age tholeiitic magmas, the reported uncertainty in magmatic thermobarometry (11–43°C, 0.1–0.4 GPa) cannot explain the temperature discrepancy present at 60 km.

Miscalculation in the forward calculation of seismic wave speeds in WISTFUL is also unlikely to explain the temperature estimate discrepancy. As we incorporate expected non-systematic uncertainty from our forward calculations into the error allowed for fitting and utilize current experimental moduli for most mineral endmembers, the only systematic error from this could be due to a difference in mixing assumptions, e.g. anisotropy. WISTFUL calculates the isotropic wave speeds, so comparing with the fast direction wave speeds would produce colder than realistic temperature estimates. As MITPS_20 inverts isotropic wave speed from combination of teleseismic body waves and surface wave arrival times, a systematic increase in recovered wave speed due to anisotropy beneath all regions with magmatic temperature estimates is unlikely.

Lastly, WISTFUL does not incorporate any effect of melt and hydrous phases, both of which would decrease the predicted temperature. Melt strongly reduces V_s (e.g., Hammond and Humphreys, 2000), but the exact wave speed reduction is heavily dependent on the melt content and the melt connectivity (Zhu et al., 2011). Thus, incorporating the effect of melt would make supersolidus temperatures require even lower wave speeds than observed. Similarly, pargasitic amphibole, ($NaCa_2(Mg_4Al)(Si_6Al_2)O_{22}(OH)_2$), the most common hydrous phase predicted for the shallow mantle (Dawson and Smith, 1982), has V_s =3.85 km s^{-1} and V_p/V_s =1.83 at 60 km pressure and 1200°C assuming the same anelasticity described in Section 3 and moduli from Abers and Hacker (2016). At the same conditions, diopside ($MgCaSi_2O_6$) has V_s =4.35 km s^{-1} and V_p/V_s =1.78. Replacing clinopyroxene at the same temperature with pargasite would decrease V_s and increase V_p/V_s (shifting all forward calculations to the upper left in Figure 2). Therefore, the addition of melt and/or hydrous phases would decrease the predicted temperature for the same seismic wave speed. Despite amphibole dikes and peridotites being hypothesized as a significant source of volatiles for alkaline and ocean-island basalts (Harry and Leeman, 1995; Pilet et al., 2011), the volume required to have a geochemical impact is unlikely to have a noticeable impact on seismic wave speed of the shallow mantle on the scale we are can interpret with MITPS_20 (˜1.5°).

In summary, our results agree within error of recent (<10 Ma) xenolith compositions, predict temperature greater or equal temperature to spinel-bearing and garnet-bearing xenoliths, but underpredict magmatic temperature estimates, especially at 60 km. The systematic difference between our best-fit temperature estimates with magmatic temperature estimates are best explained by a difference in the scale of the estimates, smearing in the tomographic models at shallow depths along a steep geotherm, and/or errors in anelastic corrections. Further experimental work on anelasticity is required to better interpret high temperature mantle regions like the western United States.

Supplementary Table 1: Compiled xenolith thermobarometry and compositional data. Empty cells represent data that was not reported or measured. All compositional data is in wt. %. References listed at the bottom of the table.

Supplementary Table 2: Locations, sources, and primary magma thermobarometry data utilized for Figure S1. Full references listed at bottom of table.

Supplemental Data File 1: This data file contains the MITPS_20 model used to produce the results presented in the paper of temperature, Mg #, and density with uncertainties at 60, 80, and 100 km depth. Variables are named following the table below.

lat	Latitude [°N]
lon	Longitude [°E]
mg60	Calculated Mg # at 60 km as described in main text
mg60_err	Calculated Mg # uncertainty at 60 km as described in main text
mg80	Calculated Mg # at 80 km as described in main text
mg80_err	Calculated Mg # uncertainty at 80 km as described in main text
mg100	Calculated Mg # at 100 km as described in main text
mg100_err	Calculated Mg # uncertainty at 100 km as described in main text
P60	Estimated pressure for each grid point at 60 km [GPa].
P80	Estimated pressure for each grid point at 80 km [GPa].
P100	Estimated pressure for each grid point at 100 km [GPa].
rho60	Calculated density at 60 km as described in main text [kg m^{-3}]
rho60_err	Calculated density uncertainty at 60 km as described in main text [kg m^{-3}]
rho80	Calculated density at 80 km as described in main text [kg m^{-3}]
rho80_err	Calculated density uncertainty at 80 km as described in main text [kg m^{-3}]
rho100	Calculated density at 100 km as described in main text [kg m^{-3}]
rho100_err	Calculated density uncertainty at 100 km as described in main text [kg m^{-3}]
T60	Calculated temperature at 60 km as described in main text [°C]
T60_err	Calculated temperature uncertainty at 60 km as described in main text [°C]
T80	Calculated temperature at 80 km as described in main text [°C]
T80_err	Calculated temperature uncertainty at 80 km as described in main text [°C]
T100	Calculated temperature at 80 km as described in main text [°C]
T100_err	Calculated temperature uncertainty at 80 km as described in main text [°C]
VpVs60	Vp/Vs from MITPS_20 at 60 km
VpVs80	Vp/Vs from MITPS_20 at 80 km
VpVs100	Vp/Vs from MITPS_20 at 100 km
Vs60	Vs from MITPS_20 at 60 km
Vs80	Vs from MITPS_20 at 80 km
Vs100	Vs from MITPS_20 at 100 km

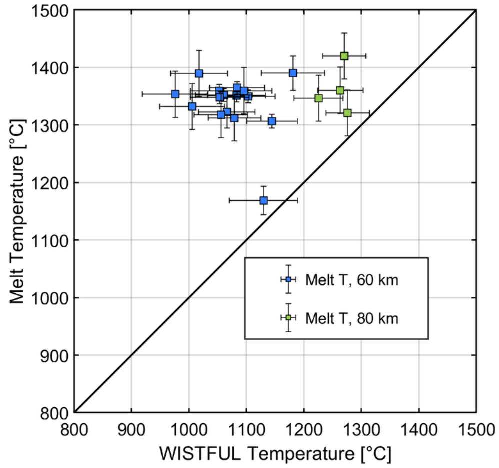

Figure S1: Temperature estimates from magmatic temperature estimates against average WISTFUL temperature within 0.5° arcdistance of the surface outcrop from Figure S3 for 60 (blue) and 80 km (green). Error bars depict a 1-sigma error.

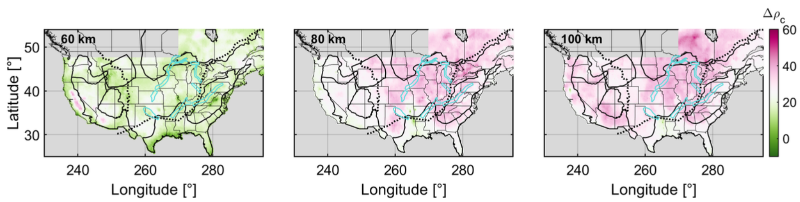

Figure S2: Compositional buoyancy as defined in section 6.2, equation 7. Boundaries as in Figure S1.

References:

Abers, G.A., Hacker, B.R., 2016. A MATLAB toolbox and Excel workbook for calculating the densities, seismic wave speeds, and major element composition of minerals and rocks at pressure and temperature. Geochemistry, Geophys. Geosystems. https://doi.org/10.1002/2015GC006171

Aizawa, Y., Barnhoorn, A., Faul, U.H., Fitz Gerald, J.D., Jackson, I., Kovács, I., 2008. Seismic properties of Anita Bay dunite: An exploratory study of the influence of water. J. Petrol. 49, 841–855. https://doi.org/10.1093/petrology/egn007

Baker, M.B., Grove, T.L., Price, R., 1994. Primitive basalts and andesites from the Mt. Shasta region, N. California: products of varying melt fraction and water content. Contrib. to Mineral. Petrol. 118, 111–129. https://doi.org/10.1007/BF01052863

Behn, M.D., Hirth, G., Elsenbeck, J.R., 2009. Implications of grain size evolution on the seismic structure of the oceanic upper mantle. Earth Planet. Sci. Lett. 282, 178–189. https://doi.org/10.1016/j.epsl.2009.03.014

Bucholz, C.E., Gaetani, G.A., Behn, M.D., Shimizu, N., 2013. Post-entrapment modification of volatiles and oxygen fugacity in olivine-hosted melt inclusions. Earth Planet. Sci. Lett. 374, 145–155. https://doi.org/10.1016/j.epsl.2013.05.033

Cline, C.J., Faul, U.H., David, E.C., Berry, A.J., Jackson, I., 2018. Redox-influenced seismic properties of uppermantle olivine. Nature 555, 355–358. https://doi.org/10.1038/nature25764

Dawson, J.B., Smith, J. V., 1982. Upper-mantle amphiboles: a review. Mineral. Mag. 45, 35–46. https://doi.org/10.1180/minmag.1982.045.337.04

Faul, U., Jackson, I., 2015. Transient creep and strain energy dissipation: An experimental perspective. Annu. Rev. Earth Planet. Sci. 43, 541–569. https://doi.org/10.1146/annurev-earth-060313-054732

Faul, U., Jackson, I., 2005. The seismological signature of temperature and grain size variations in the upper mantle. Earth Planet. Sci. Lett. 234, 119–134. https://doi.org/10.1016/j.epsl.2005.02.008

Feineman, M.D., DePaolo, D.J., 2003. Steady-state 226Ra/230Th disequilibrium in mantle minerals: Implications for melt transport rates in island arcs. Earth Planet. Sci. Lett. 215, 339–355. https://doi.org/10.1016/S0012-821X(03)00454-0

Gaetani, G.A., O'Leary, J.A., Shimizu, N., Bucholz, C.E., Newville, M., 2012. Rapid reequilibration of H 2O and oxygen fugacity in olivine-hosted melt inclusions. Geology 40, 915–918. https://doi.org/10.1130/G32992.1

Golos, E.M., Fang, H., van der Hilst, R.D., 2020. Variations in Seismic Wave Speed and VP/VS Ratio in the North American Lithosphere. J. Geophys. Res. Solid Earth 125. https://doi.org/10.1029/2020JB020574

Golos, E.M., Fischer, K.M., 2022. New Insights Into Lithospheric Structure and Melting Beneath the Colorado Plateau. Geochemistry, Geophys. Geosystems 23. https://doi.org/10.1029/2021gc010252

Grove, T., Parman, S., Bowring, S., Price, R., Baker, M., 2002. The role of an H2O-rich fluid component in the generation of primitive basaltic andesites and andesites from the Mt. Shasta region, N California. Contrib. to Mineral. Petrol. 142, 375–396. https://doi.org/10.1007/s004100100299

Hammond, W.C., Humphreys, E.D., 2000. Upper mantle seismic wave attenuation: Effects of realistic partial melt distribution. J. Geophys. Res. Solid Earth 105, 10987–10999. https://doi.org/10.1029/2000jb900042

Harry, D.L., Leeman, P., 1995. Partial melting of melt metasomatized subcontinental mantle and the magma source potential of the lower lithosphere. J. Geophys. Res. 100, 10255–10269.

Hirschmann, M.M., 2000. Mantle solidus: Experimental constraints and the effects of peridotite composition. Geochemistry, Geophys. Geosystems 1. https://doi.org/10.1029/2000GC000070

Jackson, I., Faul, U.H., 2010. Grainsize-sensitive viscoelastic relaxation in olivine: Towards a robust laboratory-based model for seismological application. Phys. Earth Planet. Inter. 183, 151–163. https://doi.org/10.1016/j.pepi.2010.09.005

Karato, S.I., Park, J., 2018. On the origin of the upper mantle seismic discontinuities, Lithospheric Discontinuities. https://doi.org/10.1002/9781119249740.ch1

Kelemen, P.B., Dick, H.J.B., 1995. Focused melt flow and localized deformation in the upper mantle: juxtaposition of replacive dunite and ductile shear zones in the Josephine peridotite, SW Oregon. J. Geophys. Res. 100, 423–438. https://doi.org/10.1029/94JB02063

Kelley, K.A., Cottrell, E., 2012. The influence of magmatic differentiation on the oxidation state of Fe in a basaltic arc magma. Earth Planet. Sci. Lett. 329–330, 109–121. https://doi.org/10.1016/j.epsl.2012.02.010

Leeman, W.P., Lewis, J.F., Evarts, R.C., Conrey, R.M., Streck, M.J., 2005. Petrologic constraints on the thermal structure of the Cascades arc. J. Volcanol. Geotherm. Res. 140, 67–105. https://doi.org/10.1016/j.jvolgeores.2004.07.016

Ma, Z., Dalton, C.A., Russell, J.B., Gaherty, J.B., Hirth, G., Forsyth, D.W., 2020. Shear attenuation and anelastic mechanisms in the central Pacific upper mantle. Earth Planet. Sci. Lett. 536, 116148. https://doi.org/10.1016/j.epsl.2020.116148

Mitchell, A.L., Grove, T.L., 2015. Melting the hydrous, subarc mantle: the origin of primitive andesites. Contrib. to Mineral. Petrol. 170, 1–23. https://doi.org/10.1007/s00410-015-1161-4

Pilet, S., Baker, M.B., Müntener, O., Stolper, E.M., 2011. Monte Carlo simulations of metasomatic enrichment in the lithosphere and implications for the source of alkaline basalts. J. Petrol. 52, 1415–1442. https://doi.org/10.1093/petrology/egr007

Plank, T., Forsyth, D.W., 2016. Thermal structure and melting conditions in the mantle beneath the Basin and Range province from seismology and petrology. Geochemistry Geophys. Geosystems 17, 1312–1338. https://doi.org/10.1002/2015GC006205.Received

Ruscitto, D.M., Wallace, P.J., Johnson, E.R., Kent, A.J.R., Bindeman, I.N., 2010. Volatile contents of mafic magmas from cinder cones in the Central Oregon High Cascades: Implications for magma formation and mantle conditions in a hot arc. Earth Planet. Sci. Lett. 298, 153–161. https://doi.org/10.1016/j.epsl.2010.07.037

Till, C.B., 2017. A review and update of mantle thermobarometry for primitive arc magmas. Am. Mineral. 102, 931–947. https://doi.org/10.2138/am-2017-5783

Till, C.B., Grove, T.L., Carlson, R.W., Donnelly-Nolan, J.M., Fouch, M.J., Wagner, L.S., Hart, W.K., 2013. Depths and temperatures of <10.5 Ma mantle melting and the lithosphere-asthenosphere boundary below southern Oregon and northern California. Geochemistry, Geophys. Geosystems 14, 864–879. https://doi.org/10.1002/ggge.20070

Venzke, E. (ed), 2013. Global Volcanism Program, 2013. Volcanoes of the World, v. 4.10.0. https://doi.org/https://doi.org/10.5479/si.GVP.VOTW4-2013

Wooley, A., 1987. Alkaline rocks and carbonatites of the world, part 1: North and South America. University of Texas Press.

Zhu, W., Gaetani, G.A., Fusseis, F., Montesi, L.G.J., De Carlo, F., 2011. Microtomography of Partially Molten Rocks: Three-Dimensional Melt Distribution in Mantle Peridotite. Science (80-.). 332, 88–91. https://doi.org/10.1126/science.1202221

Hosted file

`essoar.10512490.1.docx` available at https://authorea.com/users/523759/articles/595314-mantle-thermochemical-variations-beneath-the-continental-united-states-through-petrologic-interpretation-of-seismic-tomography

Mantle Thermochemical Variations beneath the Continental United States Through Petrologic Interpretation of Seismic Tomography

William J. Shinevar[1*], Eva M. Golos[2], Oliver Jagoutz[3], Mark D. Behn[4], Robert D. van der Hilst[3]

[1] Department of Geology & Geophysics MIT/WHOI Joint Program in Oceanography/Applied Ocean Engineering

[2] Department of Geoscience, University of Wisconsin - Madison

[3] Department of Earth, Atmospheric and Planetary Sciences, Massachusetts Institute of Technology

[4] Department of Earth and Environmental Sciences, Boston College

[*]now at Department of Geological Sciences, University of Colorado Boulder

Corresponding author: William J. Shinevar (William.Shinevar@colorado.edu)

Abstract

The continental lithospheric mantle plays an essential role in stabilizing continents over long geological time scales. Quantifying spatial variations in compositional and thermochemical properties of the mantle lithosphere is crucial to understanding its formation and its impact on continental stability; however, our understanding of these variations remains limited. Here we apply the Whole-rock Interpretive Seismic Toolbox For Ultramafic Lithologies (WISTFUL) to estimate thermal, compositional, and density variations in the continental mantle beneath the contiguous United States from MITPS_20, a joint body and surface wave tomographic inversion for V_p and V_s with high resolution in the shallow mantle (60–100 km). Our analysis shows lateral variations in temperature beneath the continental United States of up to 800–900°C at 60, 80, and 100 km depth. East of the Rocky Mountains, the mantle lithosphere is generally cold (350–850°C at 60 km), with higher temperatures (up to 1000°C at 60 km) along the Atlantic coastal margin. By contrast, the mantle lithosphere west of the Rocky Mountains is hot (typically >1000°C at 60 km, >1200°C at 80–100 km), with the highest temperatures beneath Holocene volcanoes. In agreement with previous work, we find that the predicted chemical depletion does not fully offset the density difference due to temperature. Extending our results using Rayleigh-Taylor instability analysis, implies the lithosphere below the United States could be undergoing oscillatory convection, in which cooling, densification, and sinking of a chemically buoyant layer alternates with reheating and rising of that layer.

Key Points

- MITPS_20, a joint body and surface wave tomographic model of the continental United States, is interpreted in terms of temperature, composition, and density.
- Our method predicts temperatures of 260–1430°C, compositions of Mg# 85–92, and density between 3230–3370 kg m^{-3} between 60–100 km.
- These results imply that the mantle lithosphere has enough compositional buoyancy to compensate for half the negative thermal buoyancy.

1. Introduction

The North American continent consists of amalgamated continental and arc fragments originating over the course of Earth's history (Whitmeyer and Karlstrom, 2007). To first order, observations divide the continental United States into two geologic provinces (or regions): the tectonically active western region and the stable eastern region, broadly separated by the Rocky Mountain Front. Surface strain rate is higher in the west (Kreemer et al., 2014), in line with the predominantly western locations of historical large ($M_w > 6.0$) earthquakes (Petersen et al., 2020). Surface heat flow is lowest in the eastern Archean cratons (Mareschal and Jaupart, 2013), with higher surface heat flow and Holocene volcanism in the west (Venzke, 2013). The west is dominated by high topographic relief and long-wavelength negative Bouguer anomalies, in contrast to the low-relief and short-wavelength positive Bouguer anomalies in the east (Kane and Godson, 1989). The coherence between Bouguer anomalies and topography predicts smaller elastic thicknesses in the west than in the east (Steinberger and Becker, 2018), which is consistent with the inference from seismology that the depth at which mantle seismic anisotropy aligns with absolute plate motion is shallower in the west (~80 km) than in the east (~200 km) (Yuan and Romanowicz, 2010). Mantle seismic wave speeds also differ between the two regions, with slower wave speeds in the west (Golos et al., 2020).

In the upper mantle, temperature exerts the dominant control on rheology (Hirth and Kohlstedt, 2003), density, and seismic wave speed (Shinevar et al., 2022). Thus, taken together these observations suggest elevated shallow mantle temperatures in the western US compared to those in the east (e.g., Goes and van der Lee, 2002). This variation in mantle temperature has been related to the age of the lithosphere as the lithosphere cools and thickens with time (Mareschal and Jaupart, 2013).

Re-Os dating and isotopic measurements suggest that the shallow cratonic mantle is as old as the surface rocks (e.g., Pearson, 1999). In order for cratonic mantle to remain buoyant and persist over billions of years, the density increase due to cooling has been hypothesized to be balanced by a density decrease due to the depletion of the mantle through melting—the so-called isopycnic hypothesis (Jordan, 1975). The density structure associated with the combined effects of composition and temperature is therefore vital to the force balance within the North American lithosphere (Zoback and Mooney, 2003). Petrological studies have supported the isopycnic hypothesis through density estimates from Kaapvaal xenolith compositions along modern calculated geotherms (Kelly et al., 2003), but in other cratons the density increase due to cooling may not be fully compensated by composition (Eaton and Claire Perry, 2013; Forte et al., 1995; Kaban et al., 2003; Schutt and Lesher, 2006; Shapiro et al., 1999a).

The goal of this study is to interpret the MITPS_20 seismic tomographic model (Golos et al., 2020), a recent tomographic model of the continental United States, in terms of temperature, composition, and density using WISTFUL (Whole-Rock Interpretive Seismic Toolbox For Ultramafic Lithologies) (Shinevar et al., 2022). MITPS_20 incorporates both body and surface wave data from the USArray, giving improved vertical and lateral resolution within the crust and upper mantle for both V_p and V_s compared to either data set alone. WISTFUL interprets observed seismic wave speed in terms of feasible temperature, composition, and density based on comparison to a set of reference wave speeds calculated over a range of pressure-temperature (P-T) for a database of 4485 ultramafic bulk compositions. WISTFUL incorporates an up-to-date integration of laboratory measurements of elastic moduli, new thermodynamic solution models and databases chosen to best-fit the mineral modes of well-studied mantle xenoliths, and experimental calibrations of olivine anelasticity. In this study, we first briefly discuss the methodology behind MITPS_20 and WISTFUL. We then present maps of inferred temperature, composition, and density for the continental United States and eastern Canada at 60, 80, and 100 km depth, where the MITPS_20 model is best constrained by data. To validate our methodology, we compare our results at 60 and 80 km with estimates of temperature and composition from recently erupted xenoliths and magmatism. Using the best-fit density, composition, and temperatures, we then investigate the relative chemical and thermal buoyancy of continental lithosphere. We find an imbalance in these buoyancy terms, suggesting that the continental lithosphere is density unstable. We argue that these observations could be the result of oscillatory convection, in which cooling, densification, and sinking of a chemically buoyant layer alternates with reheating and rising—resulting in laterally harmonic perturbations to the interface between the layers.

2. Geological Setting and Previous Work

Geologic mapping and geochronology show that the lithosphere west of the Rocky Mountains experienced recent orogenesis (Laramide Orogeny, 75–35 Ma, English and Johnston, 2004). Laramide compression reached as far inland as Colorado due to shallow eastward subduction of the Farallon Plate (Atwater, 1989). Since cessation of Laramide compression, the Basin and Range has undergone large-scale extension (Parsons, 2006) and the Snake River Plain/Yellowstone Plateau was formed by the impingement of the Yellowstone Plume beginning at 16 Ma (Leeman, 1982). In contrast, the plate interior last experienced internal deformation during the Neoproterozoic due to the Mid-Continent Rift (1100 Ma) and Grenville Orogeny (ca. 1300–980) (Whitmeyer and Karlstrom, 2007). More recent tectonism has occurred on the eastern margin of North America, including the Taconic (500–430 Ma), Acadian Orogeny (375–335 Ma), Alleghenian Orogeny (325–260 Ma) (Hatcher, 2010), and rifting related to the opening of the Gulf of Mexico (~200 Ma) and the opening of the central Atlantic Ocean with the intrusion of the Central Atlantic Magmatic Province (~200 Ma) (Marzoli et al., 2018).

Recent improvements in seismometer coverage, seismic tomography, and interpretation have led to many new studies of the thermochemical state of the mantle lithosphere beneath the United States. Some authors estimated the temperature of the mantle beneath the continental United States assuming a single composition, finding a lateral variation of order 500°C in temperature at the crust-mantle interface (Schutt et al., 2018) or in the upper mantle (Goes and van der Lee, 2002). Perry *et al.* (2003) utilized a topography-gravity inversion to derive a three-dimensional scaling relationship between seismic wave speed and density, and subsequently applied these relations to seismic models to estimate the temperature and chemical depletion beneath the cratonic United States. They found a temperature perturbation of ~500°C and a variation in the magnesium number (Mg#, molar Mg/(Mg+Fe)x100) of ~2 at 150 km depth. More recently, Tesauro et al. (2014) took an iterative, probabilistic approach to inverting seismic wave speed and composition using other geophysical data (e.g., topography and gravity) and found up to 800°C temperature differences and 80 kg m^{-3} density differences at 100 km depth below the continental United States. Others have utilized thermodynamic calculations to invert jointly for mantle temperature and composition, finding a maximum temperature variation of 200°C and Mg# of 89–91 below the continental United States at 100 km (Khan et al., 2011). Similarly, Afonso et al. (2016) used probabilistic joint inversions to investigate the mantle thermochemical state in the western-central United States. They integrated seismic delay times, gravity data, geoid height, topography, and heat flow and found a temperature difference of more than 500°C and Mg# of 88–92 at 55 km depth between the Rio Grande Rift and Proterozoic provinces east of the Rocky Mountain Front.

3. Methodology

Here we apply WISTFUL (Shinevar et al., 2022) to the 60, 80, and 100 km depth slices of MITPS_20 (Golos et al., 2020) (Figure 1). WISTFUL is a tool that constrains the viable temperature, rock composition, and density for a given seismic wave speed via comparison with calculated seismic wave speeds for 4485 ultramafic whole rock compositions. WISTFUL's seismic wave speeds are calculated using an updated compilation of mineral elastic moduli in tandem with Perple_X (Connolly, 2009), the Holland and Powell (2011) thermodynamic database, and the Holland *et al.* (2018) solution models to calculate mineral assemblages, but excluding the effect of melt.

The MITPS_20 tomographic model describes relative variations in V_p and V_s and is generated from a joint inversion of P, P_n, and S body wave travel time delays as well as Rayleigh wave phase velocities at periods ranging from 5–290 s. Incorporating both body and surface wave data affords good vertical and lateral resolution within the crust and upper mantle for V_p and V_s (Golos et al., 2020). Combining V_p and V_s can improve the constraints on thermal and compositional variation compared to interpretation of V_p or V_s alone (Lee, 2003). This improved vertical and horizontal resolution and the availability of jointly constrained (and similarly resolved) V_p and V_s variations make MITPS_20 an appropriate model with which to investigate the compositional and thermal variations beneath the continental United States.

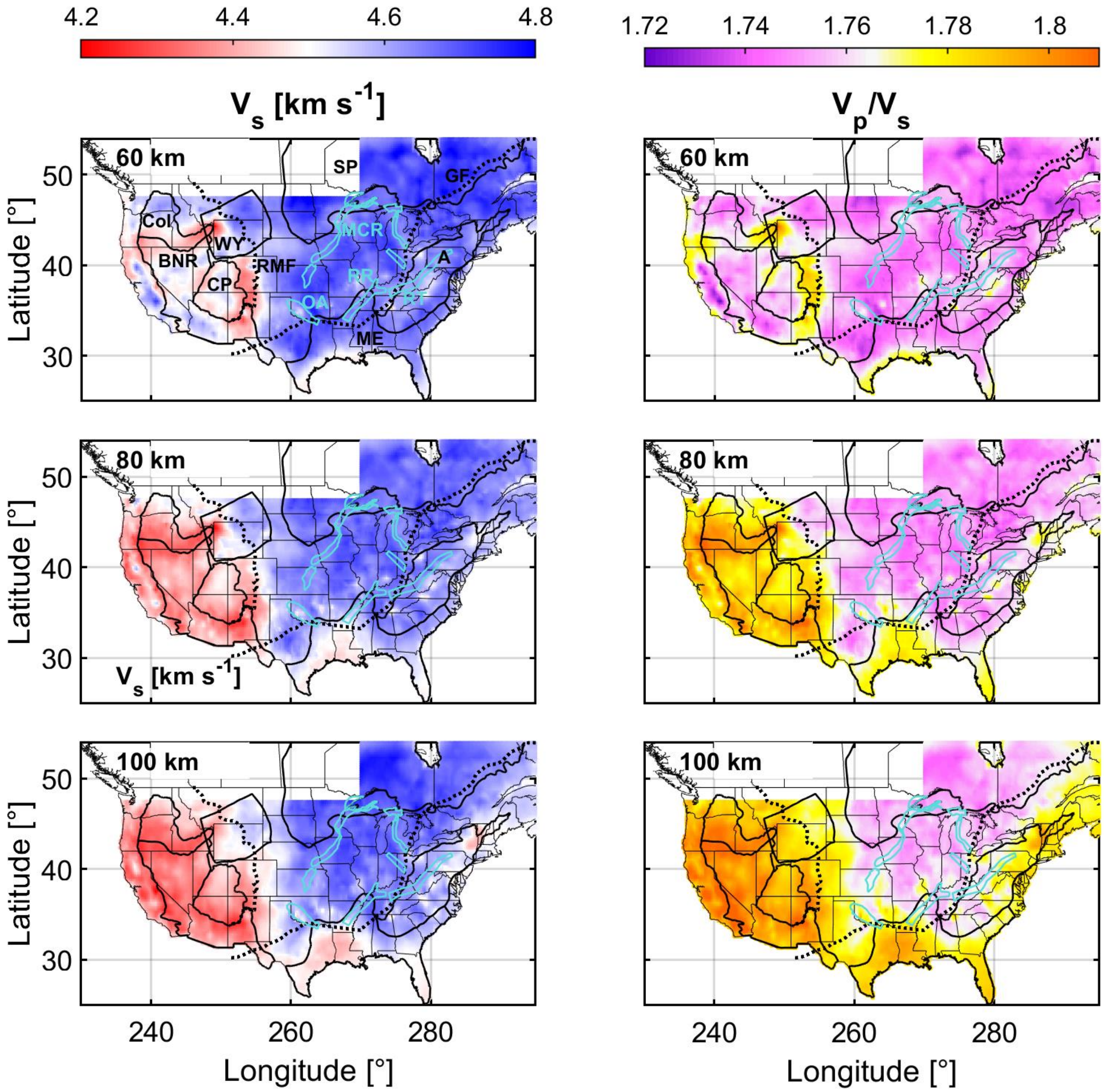

Figure 1: Depth slices of V_s (left) and V_p/V_s (right) from seismic model MITPS_20 (Golos et al., 2020) at 60 (top), 80 (middle), and 100 (bottom) km. Black boundaries represent tectonic provinces (A: Appalachian Mountains, BNR: Basin and Range, Col: Columbia Plateau/Snake River Plain, CP: Colorado Plateau, SP: Superior Craton, WY: Wyoming Craton). Cyan boundaries represent surface exposures of continental rifting events (MCR: Mid-Continent Rift, OA: Oklahoma Aulacogen, RR: Reelfoot Rift, RT: Rome Trough). The dashed lines represent the Grenville Front (GF) and the Rocky Mountain Front (RMF). Boundaries after Whitmeyer and Karlstrom (2007).

Checkerboard tests provide a qualitative diagnostic of resolution, but care must be taken with interpreting their results (Lévěque et al., 1993). We only interpret MITPS_20 in regions where recovery based on the checkerboard tests seems adequate for both V_p and V_s, thus removing western Canada. Furthermore, we limit our investigation to the 60, 80, and 100 km model depth slices, as they are the depths where V_p and V_s are best, and equally well, resolved (Golos et al., 2020). As MITPS_20 recovers 1.5°x1.5° checkerboards at 60, 80, and 100 km, we interpret anomalies of that spatial scale or larger. The map views are representative of lateral variations in wave speed in depth intervals of ± ~10 km around the indicated depth.

MITPS_20 describes relative variations in V_p and V_s (δV_p, δV_s). Inversions of synthetic data yield scaling parameters (α_p and α_s) that compensate for effects of regularization and uneven sampling, and the scaled relative variations in V_p and V_s are given by:

$$\delta V_{s_{scaled}} = \delta V_s \alpha_s, \tag{1}$$

$$\delta V_{p_{scaled}} = \delta V_p \alpha_p. \tag{2}$$

After scaling, the relative variations are converted to absolute $V_{s_{MITPS}}$ and $(V_p/V_s)_{MITPS}$ (Figure 1a, b) using

$$V_{s_{MITPS}} = \left(1 + \delta V_{s_{scaled}}\right) V_{s_{ref}} \tag{3}$$

$$(V_p/V_s)_{MITPS} = \left(1 + \frac{\delta V_{p_{scaled}}^2}{V_{s_{ref}}} - \frac{\delta V_{s_{scaled}}^2 V_{p_{ref}}}{V_{s_{ref}}^2}\right)(V_p/V_s)_{ref}, \tag{4}$$

Where $V_{p_{ref}}$and $V_{s_{ref}}$ are from a modified version of the *ak135* reference model (Kennett et al., 1995). $V_{p_{ref}}/V_{s_{ref}}$ for *ak135* is greater than interpretable values obtained from WISTFUL (e.g., *ak135* V_p/V_s is 1.793 at 60 km, whereas the range produced by WISTFUL is 1.73–1.77, Figure 2). Therefore, we choose independent reference values ($(V_p/V_s)_{ref}$ =1.774 at 60 km, 1.773 at 80 km, 1.781 at 100 km). Increasing $(V_p/V_s)_{ref}$ from these values has minor effects on the inferred temperature, but decreases the predicted Mg#. We choose our reference values to minimize compositional error when comparing our results against young (<10 Ma) xenolith compositions (See Section 5.1).

To interpret these seismic wave speeds in terms of temperature, density, and composition, we utilize the Number-Within-Error methodology from WISTFUL. In this approach, pressure is first calculated at each point using inferred crustal thickness from Schmandt et al. (2015) with an average crustal density of 2800 kg m^{-3} and an average mantle density of 3300 kg m^{-3}. This results in pressures of ~ 1.7, 2.4, and 3.0 GPa at 60, 80, and 100 km depth, respectively. Using the calculated pressure at each grid point, we then calculate the number of peridotites in the WISTFUL database with Mg# > 85 within 0.5% distance of the given V_s value and 0.5% of the given V_p/V_s value for all temperatures between 300 and 1600˚C. We use 0.5% because that is the error estimated for forward calculations in WISTFUL and is greater than the median uncertainty from MITPS_20 (~0.2% in V_p and V_s based on bootstrapping analyses, Golos et al., 2020).

Mg# is an estimate of melt depletion in the mantle, with more depletion resulting in a higher Mg# due to the preference of FeO to partition into melt. Peridotite xenolith compositions range from Mg# 86–95, and most primitive mantle estimates range from Mg# 89–90 (Workman and Hart, 2005). There is a correlation between Mg# and V_p/V_s for peridotites within the garnet-stability field; peridotites that are more depleted have a lower V_p/V_s (Afonso et al., 2010; Lee, 2003). This correlation is weaker in the spinel-stability field, making the interpretation more non-unique at 60 km depth and at high temperatures due to the pronounced effect of anelasticity (Afonso et al., 2010).

The best-fit temperature and uncertainty are defined as the mean and standard deviation of a Gaussian distribution fit to the number of samples within error over all temperatures (300–1600°C). The best-fit composition or density and its uncertainty are defined as the mean and standard deviation at the best-fit temperature of all the peridotites that fit a given V_s and V_p/V_s, weighted by the inverse of the total misfit, X

$$X = \sqrt{\left(\frac{V_{s_{MITPS}} - V_{s_{WISTFUL}}}{V_{s_{MITPS}}}\right)^2 + \left(\frac{(V_p/V_s)_{MITPS} - (V_p/V_s)_{WISTFUL}}{(V_p/V_s)_{MITPS}}\right)^2} \qquad (5)$$

where ($V_{s_{MITPS}}$, $(V_p/V_s)_{MITPS}$) and ($V_{s_{WISTFUL}}$, $(V_p/V_s)_{WISTFUL}$) are the seismic wave speeds and ratios for MITPS_20 and the WISTFUL peridotites, respectively. Temperature, density, and composition estimates are only calculated for wave speeds that have at least 20 rock samples wave speeds within error. This procedure is repeated for every point in the seismic model to generate temperature, composition, and density maps. For a given V_s, a lower V_p/V_s will generally predict a more depleted composition (Figure 2), but the magnitude of this effect depends on temperature and absolute seismic wave speeds.

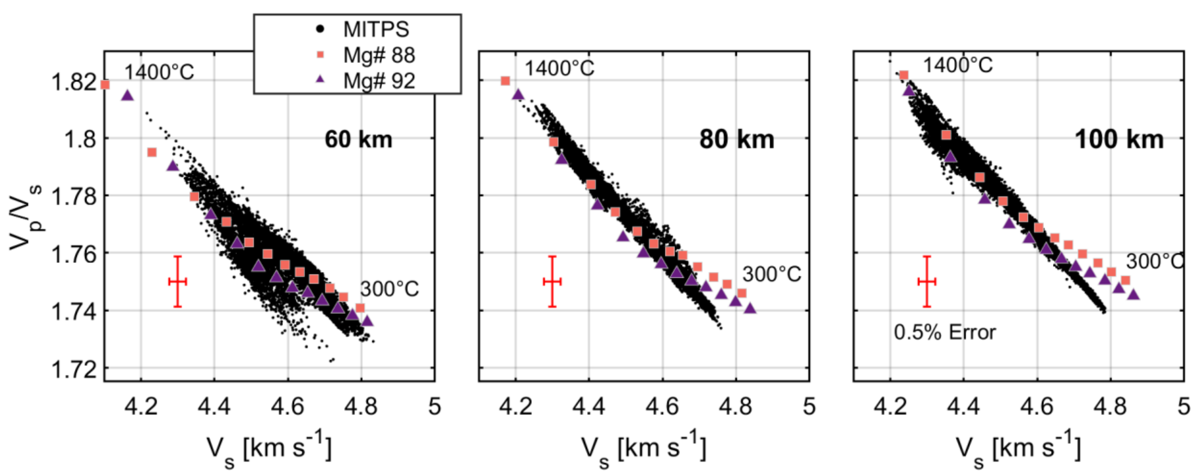

Figure 2: Seismic wave speeds from MITPS_20 at 60 (left), 80 (middle), and 100 (right) km depth plotted alongside average wave speeds for enriched (Mg#=88, pink squares) and depleted (Mg#=92, purple triangles) peridotites from 300 to 1400°C plotted every 100°C assuming the Behn *et al.* (2009) power-law anelasticity. Red error bars represent the estimated 0.5 % error for the WISTFUL forward calculations.

In order to interpret seismic wave speeds under mantle conditions, we correct for the anelastic behavior of olivine at high temperatures using the power-law formulation of Behn *et al.* (2009). We assume that olivine anelasticity applies to all minerals present. We apply anelastic corrections using the periods that dominate surface wave sensitivity for MITPS_20 (38 s for 60 km, 45 s for 80 km, and 57s for 100 km). We assume a grain size of 1 cm, in line with grain sizes for cratonic xenoliths (e.g., Baptiste and Tommasi, 2014) and Cenozoic xenoliths from the western United States (Li et al., 2008). We assume an olivine water content of 50 H/10^6 Si (~7 ppm H_2O) to approximate dry mantle peridotite, in line with average olivine water contents observed in continental mantle xenoliths from the western United States (e.g., Li et al., 2008). We note that the results and conclusions presented below do not critically depend on the precise values of grain size and water content.

4. Results

Our methodology predicts the mantle beneath the Northern Cordillera United States to be hot relative to the central and eastern United States (Figure 3, Table 1, Supplementary Dataset 1). The lowest temperatures at each depth slice are found below the Archean Superior Province. The cratonic United States west of the Grenville Front and east of the Rocky Mountains is relatively cold, but lateral variations in temperature appear substantial (450–1000°C, 80 km). The highest predicted temperatures in the eastern interior correlate with features related to rifting (cyan lines, Figure 3). West of the Rocky Mountain Front, temperatures are elevated compared to the cratonic United States (>1200°C at 80 km). These temperatures agree with receiver function and global seismic tomographic studies that infer Lithosphere-Asthenosphere Boundary (LAB) depths shallower than 80 km in the western continental United States (Hopper and Fischer, 2018; Steinberger and Becker, 2018; Yuan and Romanowicz, 2010). Higher temperatures (1050–1400°C at 80 km) tend to align with locations of Holocene volcanism in the western United States (triangles, Figure 3, orange bars, Figure 4, Venzke, 2013) and with Cambrian or younger (<540 Ma) alkaline and carbonatite rocks (circles, Figure 3). This is expected as alkaline and carbonatite rocks derive from high-pressure and/or volatile-rich mantle melting (Wooley, 1987) and are often associated with intraplate volcanism due to rifting or plumes.

Compositionally, the cratonic United States is slightly depleted (Mg# ~91) compared to the asthenospheric mantle west of the Rocky Mountains (Mg# 89–90) at 80 and 100 km depth (Figure 5). Density correlates negatively with temperature, with the highest densities beneath Archean cratons (~3350 kg m^{-3}) and lowest west of the Rocky Mountains (~3260 kg m^{-3}) (Figure 6). Furthermore, to first order mantle densities negatively correlate with large-wavelength topography (Spearman correlation coefficient between topography and mantle densities of -0.50, -0.47, and -0.48 for 60, 80 and 100 km respectively, all $p=0$). The Spearman rank correlation coefficient detects any type of monotonic correlation rather than a sole specific functional correlation and is less sensitive to outliers. Values of r range from −1 to 1, with larger absolute values indicating that the two variables more strongly co-vary according to a monotonically increasing (positive) or decreasing (negative) relationship. The corresponding p-value indicates the probability that the relationship is due to randomness. This correlation between mantle density and topography is in agreement with the hypothesis that the western United States is near isostatic equilibrium and that mantle density variations due to temperature partially support topography (e.g., Molnar et al., 2015). It is important to note that the temperature errors are small compared to the total predicted variation (60°C error for a variation of ~1000°C), but the errors for Mg# (1.0 for a 3–7 variation) and density (20 kg m^{-3} for a 110–140 kg m^{-3} variation) can be a significant fraction of the total variations.

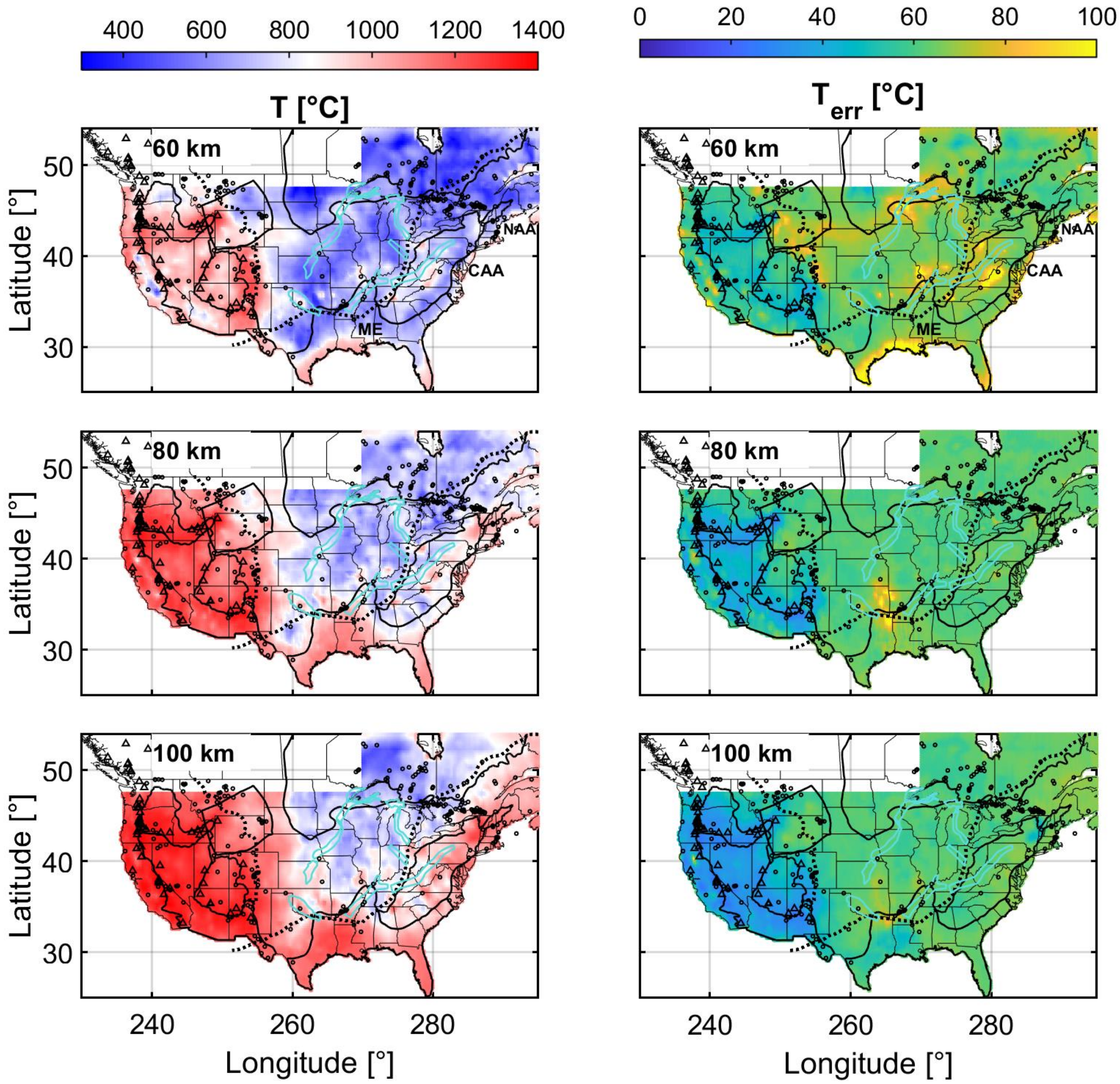

Figure 3: Best-fit temperature (left) and uncertainty (right) at 60 (top), 80 (middle), and 100 (bottom) km. Boundaries as in Figure 1. Circles represent surface outcrops of alkaline or carbonatite magmatism younger than 1 Ga (http://alkcarb.myrocks.info/, Wooley, 1987)). Triangles represent locations of Holocene volcanism (Venzke, 2013). Acronyms as follows: NAA, North Appalachian Anomaly, CAA, Central Appalachian Anomaly, ME, Mississippi Embayment. CAA and NAA text plotted 7° east of actual anomalies.

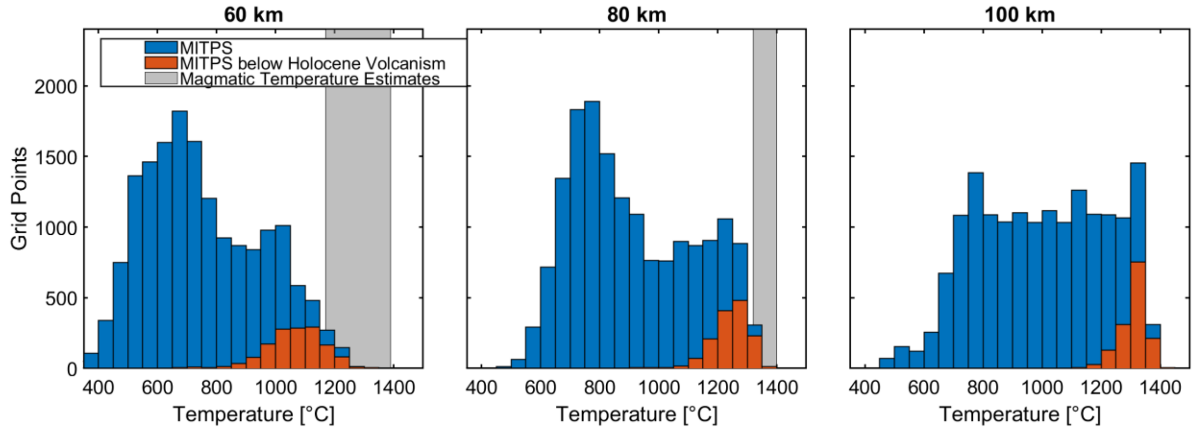

Figure 4: Temperature estimates for MITPS_20 grid points at 60 (left), 80 (middle), and 100 (right) km depths (blue) plotted along with temperature estimates within 1° arc distance of locations for Holocene volcanism (orange). Grey regions depict the range of magmatic temperature estimates (see text for discussion).

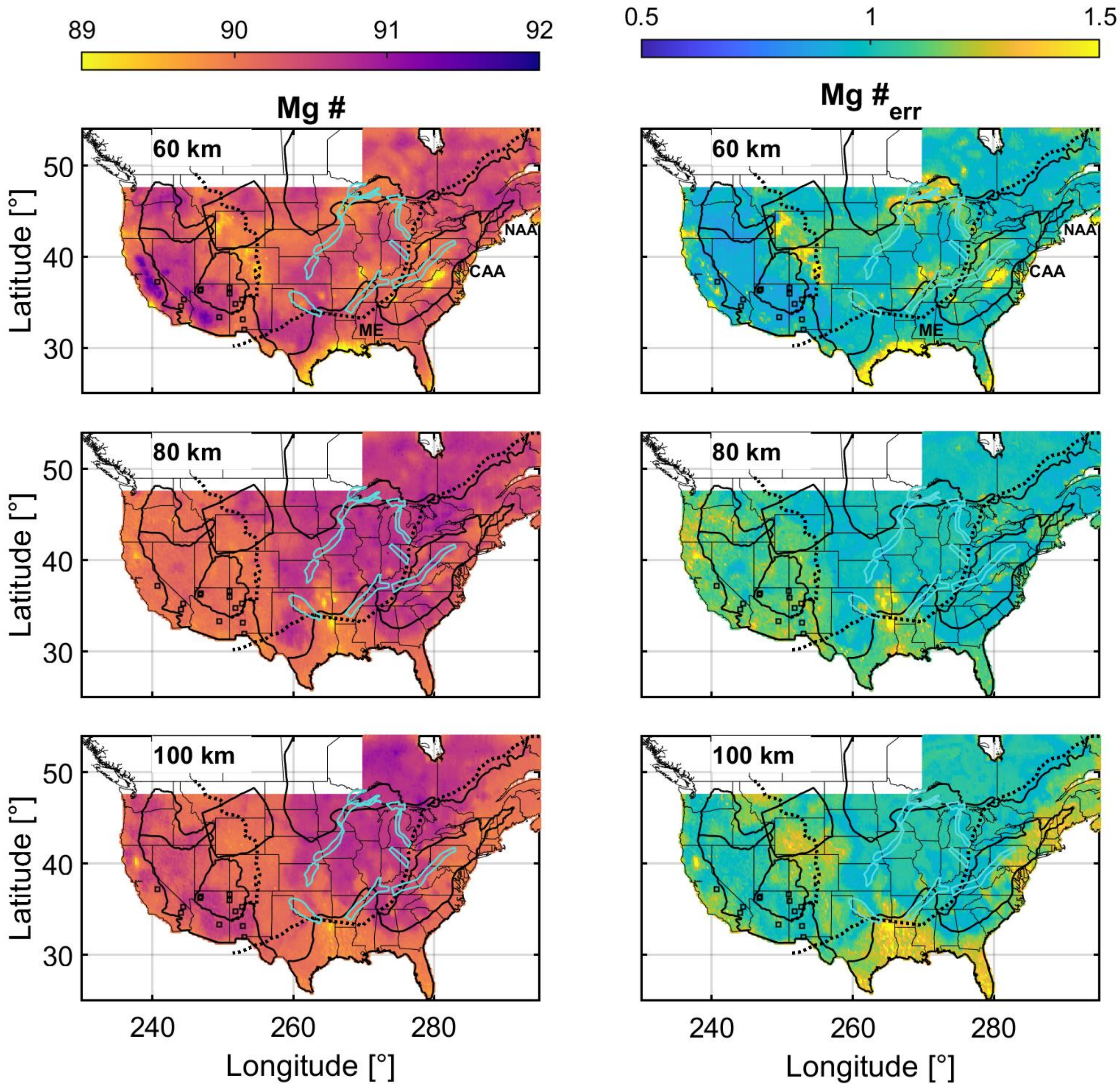
89
90
91
92
Mg #
0.5
1
1.5
Mg #err
60 km
80 km
100 km
NAA
CAA
ME
Latitude [°]
50
40
30
240
260
280
Longitude [°]

275

Figure 5: Best-fit whole rock Mg# (left) and uncertainty (right) at 60 (top), 80 (middle), and 100 (bottom) km. Boundaries as in Figure 1. Squares depict xenolith localities younger than 10 Ma.

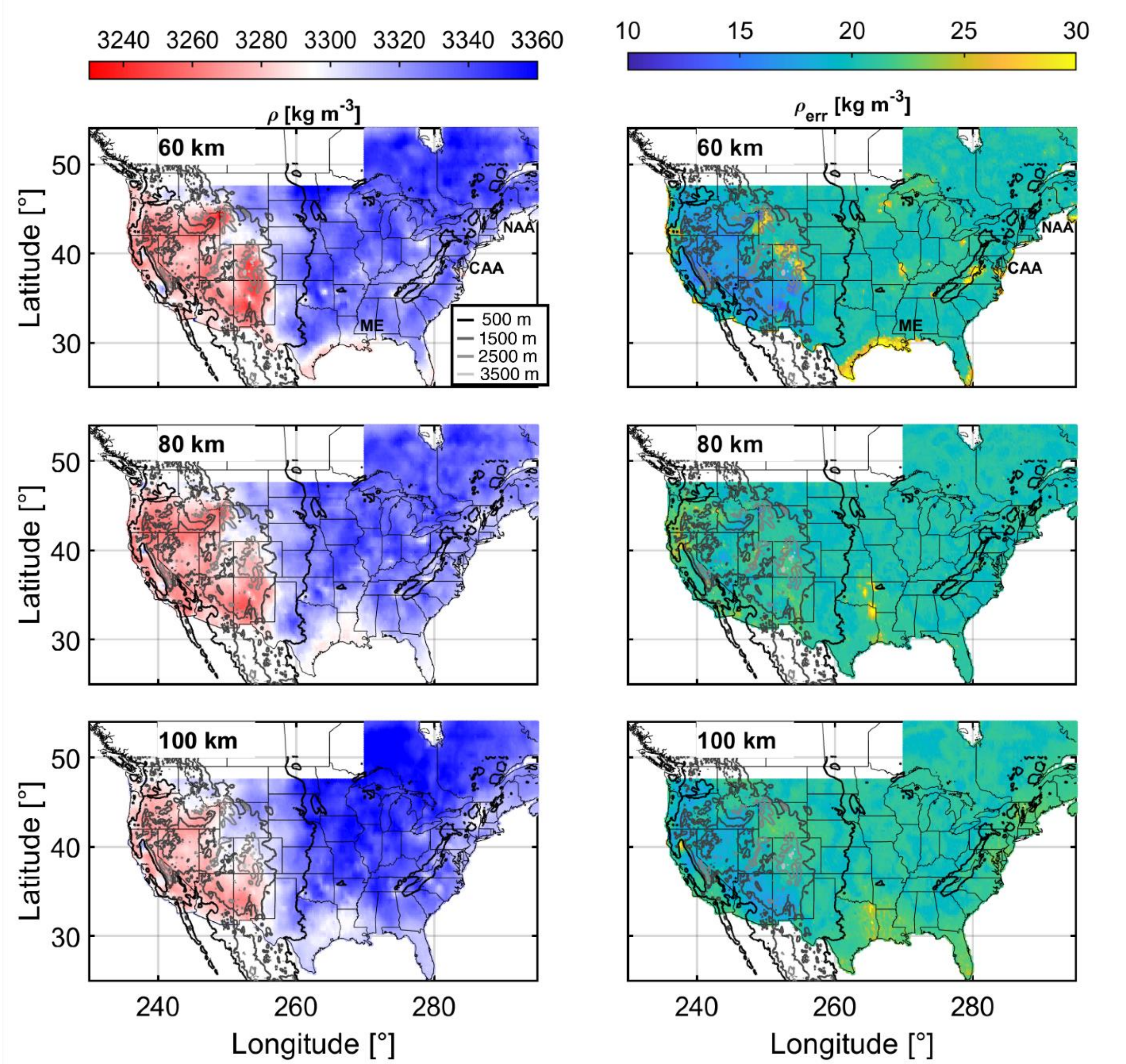

Figure 6: Best-fit density (left) and uncertainty (right) at 60 (top), 80 (middle), and 100 (bottom) km. Lines contour topography from 500–3500 m.

Depth [km]	T [°C]	Mg#	ρ [kg m^{-3}]	$\Delta\rho_c$ [kg m^{-3}]	B
60 (west of 255°)	450–1350, 1000, 60	85.0–91.7, 90.3, 1.0	3230–3350, 3280, 20	-44–42, 18	-0.72–1.95, 0.37
60 (east of 255°)	260–1200, 670, 70	87.0–91.0, 90.2, 1.1	3250–3320, 3330, 20	-25–28, 17	-0.36–0.66, 0.18
80 (west of 255°)	780–1390, 1180, 50	89.2–90.8, 90.1, 1.1	3260–3320, 3280, 20	14–26, 38	0.40–6.7, 1.25

80 (east of 255°)	440–1280, 820, 60	87.3–91.3, 90.4, 1.0	3270–3360, 3320, 20	2–48, 31	0.03–2.10, 0.44
100 (west of 255°)	960–1430, 1260, 40	88.5–90.8, 90.3, 1.1	3260–3330, 3290, 20	7–43, 31	0.22–7.16, 1.98
100 (east of 255°)	450–1290, 910, 60	88.6–91.2, 90.3, 1.1	3290–3370, 3330, 20	6–52, 32	0.19–2.83, 0.61

Table 1: Range, mean, and mean 1σ uncertainty for results at 60, 80, and 100 km east and west of 255° for T, Mg#, and ρ as well as range and mean of values for $\Delta\rho_c$ and B (see Section 6.2).

5. Method Validation

To validate our approach, we compare our results with estimates of temperature and composition from xenoliths, as well as melting P-T estimates calculated from primary magmas. The benefit of comparison with well-studied young (<10 Ma) xenoliths is that they directly constrain composition. In addition to composition, estimates of mantle temperature have been calculated from xenolith using appropriate thermobarometry. Comparison with thermobarometry using primary magma compositions is discussed in Supporting Information and Supplemental Figure 1. Another avenue for validation would be to compare our results with surface heat flow, but we forego this route due to the large uncertainties in crustal heat production and the effect of upper crustal hydrothermal processes, the dominant controls on surface heat flux (Mareschal and Jaupart, 2013).

5.1 Xenolith Compositions

We compiled 15 xenolith localities from recently erupted volcanos (<10 Ma, black squares, Figures 5, 6), and which have at least four xenolith bulk rock compositions with Mg#>85 and <2 wt % loss on ignition to avoid averaging xenoliths that have been refertilized or altered before/during eruptive processes (references in Supplementary Table 1). We assume that the average xenolith composition represents the mantle composition beneath that location and use the standard deviation as the related uncertainty. To compare the chemical compositions from xenoliths with the composition calculated from wave speeds, we average the later for all grid points within 0.5° arc-distance from the specific xenolith locality. We estimate the WISTFUL uncertainty to be the maximum of the average uncertainty or the standard deviation of the averaged results. Spinel xenolith compositions are compared with the estimated 60-km composition (blue squares, Figure 7a), while higher pressure garnet xenoliths are compared with the 80-km composition (green square, Figure 7a). Our results are within uncertainty for 14 of the 15 localities (RMSE=0.38), indicating that our method provides realistic estimates of mantle composition.

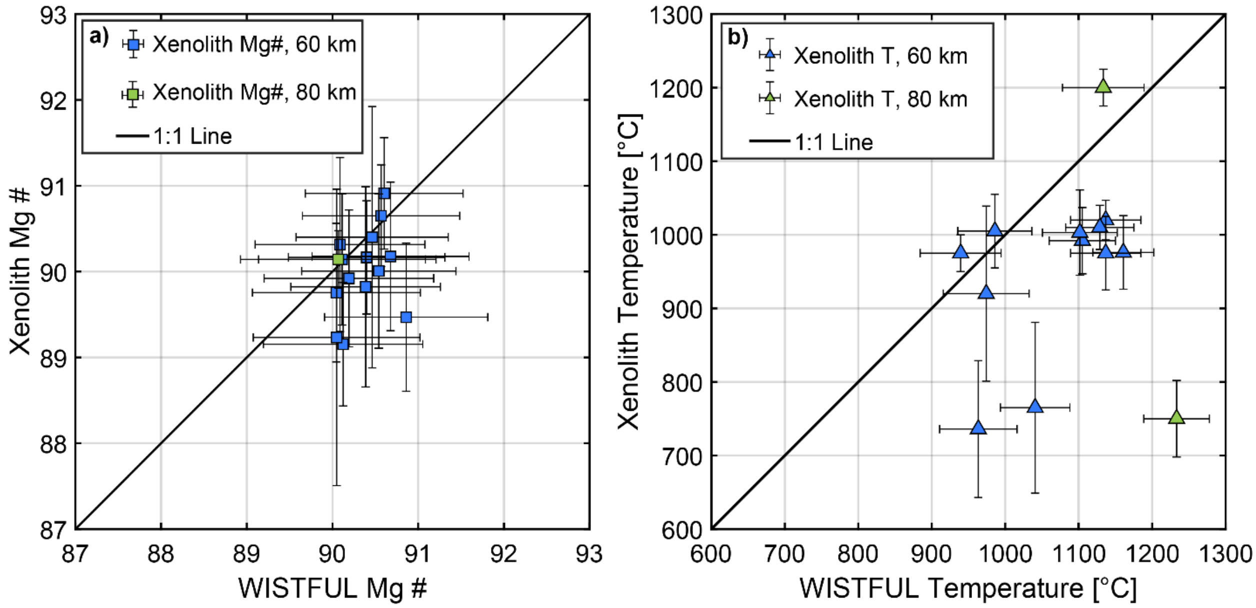

Figure 7: a) Comparison of average <10 Ma xenolith composition against average best-fit composition within 0.5° arc distance from the surface exposure. blue squares represent spinel-bearing xenolith localities for which the 60 km depth slice was used; the green square signifies a garnet-bearing xenolith locality for which the 80 km slice was used. b) Temperature estimates from xenoliths against average WISTFUL temperature within 0.5° arc distance of the surface outcrop for 60 (blue) and 80 km (green). Error bars depict a 1-σ error.

5.2 Xenolith Thermobarometry

Mantle xenolith thermobarometry relies on using the relative mineral composition to calculate the equilibrium P-T. We compiled 13 localities with at least one temperature (or P-T) estimate (references in Supplementary Table 1). Because no reliable spinel barometer exists, most spinel thermometry is calculated at 1.5 GPa as spinel-bearing xenoliths could originate anywhere in the spinel stability field (~0.7–2 GPa). Here, we compare all spinel thermometers with our 60-km estimate (~1.7 GPa) and acknowledge that our temperature estimates should be equal to or exceed the estimates from this thermometry as the spinel xenoliths could be sampling a shallower mantle. Reliable barometers exist for garnet-bearing peridotites, and we compare all temperatures from garnet-bearing peridotites within 0.3 GPa of the 80 km pressure (~2.4 GPa). To compare these temperature estimates with ours, as above, we average the best-fit temperatures from all results within 0.5° arc-distance from the locality. As with composition, we take the WISTFUL temperature error to be the maximum of the average temperature uncertainty and the standard deviation of averaged temperatures. We consider the temperature error in a xenolith locality to be the maximum of the standard deviation of the calculated temperatures and published thermometer uncertainty.

Our temperature estimates agree within error for 4 out of 11 spinel xenolith localities, while overpredicting temperature by ~125°C for five xenolith localities (Figure 7b). Xenoliths from Green Knobs in New Mexico and Vulcan's Throne in Arizona predict much lower temperatures (750–775°C) at 60 km than our results (~1000°C). These values appear to be anomalously low as there is recent (<1 Myr) magmatism nearby and recently exhumed granulite facies lower crustal xenoliths (Cipar et al., 2020). It is therefore possible that these spinel xenoliths sample significantly shallower mantle, potentially as shallow as the regional Moho (~30 km, Schmandt et al., 2015).

Our results disagree within error for both garnet xenolith localities (green triangles, Figure 7b). The more enigmatic garnet-bearing xenolith locality (Big Creek, Sierra Nevadas, California) predicts low temperatures for 80 km (~750°C), in stark disagreement with our results. It is unlikely that these xenoliths were not in equilibrium at high temperatures (~750°C). Instead, the xenoliths may record a no-longer-present thermochemical state, as they erupted in an 8 Myr old diatreme (Chin et al., 2012) in a region hypothesized to be undergoing continental delamination between 10–3 Ma (Zandt et al., 2004).

6. Discussion

Here we discuss regions with anomalous temperature and composition to compare with regional geology and tectonic history. Subsequently, we present estimates of lithospheric buoyancy, and consider implications for our understanding of cratonic lithospheric stability.

6.1 A cross-country tour of lithospheric temperature and composition

6.1.1 Eastern United States Margin

The lithospheric mantle between the Grenville Front and the Atlantic and Gulf coasts is uniformly hotter than the cratonic regions further west (700–1200°C at 80 km, and 750–1300°C at 100 km). At these depths the eastern coastal regions are compositionally more similar (Mg# ~90) to the mantle west of the Rocky Mountains than the slightly more depleted cratonic regions in between (Mg# ~91). At 60 km, the Atlantic coastal margin achieves the highest temperatures in three large (>2°x2°) regions: (1) the Central Appalachian Anomaly below Virginia and West Virginia, (2) the North Appalachian Anomaly below New York and New England, and (3) the Mississippi Embayment.

The Central Appalachian Anomaly (CAA) reaches temperatures up to 1000±90°C at 60 km and 1200±60°C at 80 km, which is substantially higher than the surroundings which is typically 700–900°C. Furthermore, this is one of the most fertile regions beneath the continental US (Mg# <89±1.5 at 60 km), though the compositional anomaly is smaller at greater depth. This high temperature is consistent with Eocene-aged (~48 Ma) basaltic dike swarms in Virginia and West Virginia, which record Eocene P-T conditions of 1412 ± 25°C and 2.32 ± 0.31 GPa, ~80 km depth (Mazza *et al.*, 2014). The CAA has been hypothesized to result from asthenospheric upwelling driven by delamination (Mazza et al., 2014), edge-driven convection (Mustelier and Menke, 2021), or thermal remnants of Atlantic rifting and the Central Atlantic Magmatic Province (Marzoli et al., 2018).

The North Appalachian Anomaly (NAA) has elevated temperatures of up to 950±90°C at 60 km, 1100±70°C at 80 km, and 1250±60°C at 100 km. In view of the low seismic shear wave speeds and a decrease in the strength of mantle anisotropy, the NAA has been interpreted to be the result of a mantle upwelling (Levin et al., 2018; Yang and Gao, 2018). The lack of observed surface volcanism suggests that the upwelling is relatively recent (Levin et al., 2018). Yang and Gao (2018) hypothesized that the source of this anomaly is related to, or caused by, the Great Meteor Hotspot, which traversed from Southeastern Canada to New England, formed the Cretaceous White Mountains intrusive suite in New Hampshire (~130–100 Ma), and more recently created the New England Sea Mounts (100–80 Ma). Conversely, Menke *et al.* (2016) hypothesized that this feature is caused by edge-driven convection. The elevated lithospheric temperature we infer at this anomaly is consistent with a locally thinned lithosphere and asthenospheric upwelling, but our analysis cannot constrain the cause of upwelling.

Lastly, the Mississippi Embayment (ME) is a large region that has experienced subsidence beginning in the late Cretaceous (ca. 90 Ma, Cox and Van Arsdale, 2002) . The mantle beneath this region shows distinctly higher temperatures at 80 km (1100±50°C) and 100 km (1250±50°C) than the rest of the United States east and south of the Grenville Front. Similarly, it is more enriched than the cratonic US at all depths (Mg# 89–90±1.5). The highest temperatures in the ME are located below Louisiana (up to 1200°C at 80 km and 1350°C at 100 km). At 60 km depth, the temperatures are similar to the cratonic interior (500–800°C) with the exception of the southern fringe of Texas and Florida. To explain the subsidence, some authors have invoked renewed extension related to the opening of the Gulf of Mexico (e.g., Braile *et al.*, 1984). The embayment could also be related to an increased heat flux from the Bermuda hotspot below Mississippi at the beginning of the subsidence (Cox and Van Arsdale, 2002). This increased flux, along with the beginning of seafloor spreading in the Gulf of Mexico (~150 Ma), would be consistent with the elevated temperatures observed here and inferred from other seismic analyses (Krauss and Menke, 2020).

6.1.2 Central United States

Within the central US, sites of rifting have no thermal and compositional anomalies compared with their surrounding mantle. Mid-to-late Cambrian rifting (550–500 Ma) is expressed in features such as the Rome Trough, Reelfoot Rift, and Oklahoma aulacogen (e.g., Brueseke et al., 2016). We find that these features and the Proterozoic Mid-Continent Rift (1,100 Ma, MCR) are not correlated with elevated temperatures compared to their surroundings as expected given their age (900–1000°C at 60 and 80 km, cyan outlines, Figure 3), Compositionally, these regions also are within error the same as surrounding regions, with slightly greater variations at 60 km (Mg# 89–90±1.2).

6.1.3 Western United States

The hottest regions in the western US (>1200°C at 60 km) are associated with recent volcanism (Figure 4) and/or rifting, such as the Rio Grande Rift, the Yellowstone/Snake River Plain hotspot track, as well as the Cascade Range and related back-arcs, including Oregon's High Lava Plains. The Basin and Range is colder at 60 km (900–1000ºC) than most areas with Holocene volcanism (800–1200°C), but has similar temperatures at 80 km depth (~1200ºC).

The lowest mantle temperatures (<700°C) in the western US are found in the eastern Wyoming Craton, the Isabella Anomaly in California, and southeastern Washington and Idaho.

At 80 and 100 km, the mantle below the eastern Wyoming Craton is 200–400°C colder than the western Wyoming Craton. Furthermore at 60 and 80 km, the western Wyoming craton is enriched by ~1 Mg# compared to the eastern Wyoming craton. This could signify that the western portion has been modified by the Yellowstone hotspot and the Laramide orogeny as previously hypothesized (Dave and Li, 2016). The low temperatures and depleted mantle compositions (Mg# >91±1) under California at 60 km are predicted based on higher V_s (>4.5 km s^{-1} at 60 and 80 km) and lower V_p/V_s (<1.75 at 60 and 80 km) relative to the regional average and could be explained by either an overthickened or delaminating eclogitic lower arc crustal root (Bernardino et al., 2019) or a remnant, unsubducted portion of the Farallon slab (Wang et al., 2013). Similar wave speeds indicate low temperatures and depleted composition (Mg# 91±0.9) in southeastern Washington and Idaho. This anomaly has been hypothesized to be caused by a remnant hanging slab (Schmandt and Humphreys, 2011). Alternatively, the high wave speeds could indicate a mantle relatively unaffected by volcanic processes, similar to the eastern Wyoming craton. This would be consistent with the lack of recent volcanism (Figure 3).

6.1.4 Rocky Mountain Front

Basal tractions are likely high in the mantle beneath the Rocky Mountain Front, where our methodology predicts large horizontal density and temperature gradients (Figure 7). Shapiro *et al.*, (1999b) found that the deep lithosphere was stable in the presence of basal tractions as long as there existed some combination of compositional buoyancy and high mantle activation energies (~500 kJ/mol) comparable to those of dry olivine dislocation creep (Hirth and Kohlstedt, 2003). Similarly, Currie and Van Wijk (2016) found that in the absence of a mantle wind, a steep gradient in lithospheric thickness was stable if the cratonic mantle was dry (rheologically strong) and had a moderate compositional buoyancy, defined as the difference in density between asthenosphere and lithosphere at the same P-T conditions ($\Delta\rho_c$=20–40 kg m^{-3}). These moderate buoyancy values are consistent with our estimates of the compositional density difference between the mantle beneath the eastern Archean cratons and mantle west of the Rocky Mountains ($\Delta\rho_c$≈30 kg m^{-3}, 80 km, Table 1, Supplemental Figure 2, Section 6.2). Furthermore, edge-driven convection adjacent to a compositionally buoyant, strong cratonic lithosphere predicts mantle upwelling ~200 km away from steep lithospheric gradients (Figure 12b in Currie and Van Wijk, 2016). This would predict such an upwelling to occur beneath the Rocky Mountains, consistent with the presence of Cenozoic alkaline-carbonatite magmatism that suggests deep mantle melting (Figure 3, Wooley, 1987). Basal tractions are unlikely to support the excess 2 km of modern topography of the Rocky Mountains compared to the Great Plains, given the low regional isostatic gravity anomalies (Molnar et al., 2015). The excess topography of the Rocky Mountains is instead more likely due to a steep decline in density (~30 kg m^{-3}, ~1%), observed here beginning at the eastern front of the Rocky Mountains (~255° E, Figure 6), as previously hypothesized and inferred (e.g., Levandowski et al., 2014).

6.2 Lithospheric Buoyancy and Stability

As WISTFUL predicts temperature, density, and composition, we have the unique opportunity to investigate the relative importance of compositional and thermal buoyancy for the stability of the mantle lithosphere beneath the entire continental United States. To investigate this, we calculate a dimensionless buoyancy number, B, the ratio of the intrinsic (compositional) and thermal buoyancies,

$$B = \frac{\Delta\rho_c}{\Delta\rho_T} \tag{6}$$

where $\Delta\rho_c$ is the density variation attributed to compositional heterogeneity and $\Delta\rho_T$ is the change of density due to temperature differences (Shapiro et al., 1999b). Negative B values imply negative compositional buoyancy. A B value of 0 implies that no compositional buoyancy exists. A B value of 1 implies that the compositional and thermal effects are equal (the isopycnic hypothesis). A B value much greater than 1 implies that the compositional buoyancy is greater than thermal effects. Thus, when B>1, the compositional effect on density is sufficient for the lithosphere to remain positively buoyant, but when B<1 there will not be sufficient compositional buoyancy to overcome the negative thermal buoyancy of the cold lithospheric mantle.

We calculate B using the WISTFUL predictions of density for the compositions that are within error seismically at the best-fit temperature (Table 1). We define

$$\Delta\rho_c = \rho_{DMM} - \rho_{pot,} \tag{7}$$

where ρ_{pot} is the average density of the best-fit compositions at the same pressure and a mantle potential temperature (1350°C) weighted by the inverse of the seismic error at the best fit-temperature, and ρ_{DMM} is the density calculated for depleted MORB mantle (DMM, Mg# 89.4, Workman and Hart, 2005) at the same conditions as ρ_{pot} and utilizing the same thermodynamic calculations as WISTFUL (3245 kg m^{-3} at 60 km, 3280 kg m^{-3} at 80 km, and 3305 kg m^{-3} at 100 km). We define

$$\Delta\rho_T = \rho_{WIST} - \rho_{pot,} \tag{8}$$

where ρ_{WIST} *is* the best-fit density at the best-fit temperature. At high temperatures approaching the mantle potential temperature, $\Delta\rho_T$ becomes very small, which results in extremely large values of B. We therefore only calculate B at temperatures less than 1300°C (50°C below the reference potential temperature).

Across North America the lithospheric mantle is compositionally buoyant (B>0; Figure 8). At 60 km, B is bimodal, with low values (~0.2) east of the Rocky Mountains and slightly higher values west of the Rocky Mountains (~0.4). At 80 and 100 km, B is >1 west of the Rocky Mountains (Figure 8). The cratons in the eastern United States have B values between 0.35 and 0.55 at 80 and 100 km, suggesting that the density increase due to cooling is not fully counteracted by chemical depletion. This result agrees with previous estimates from seismology (Forte et al., 1995), long-wavelength geoid (Shapiro et al., 1999a), gravity (Kaban et al., 2003), geochemical density estimates (Schutt and Lesher, 2006), and thermal models (Eaton and Claire Perry, 2013), all which find that B for cratonic roots is typically a positive value less than 1. East of the Grenville Front, B increases with depth (~0.2 at 60 km, 0.4 at 80 km, and 0.4–>1 at 100 km). Our results predict that while the shallow (60 km) mantle lithosphere is not isopycnic, the deeper (>80 km), high temperature lithosphere (>1100°C) is isopycnic and should be stable without external forcing.

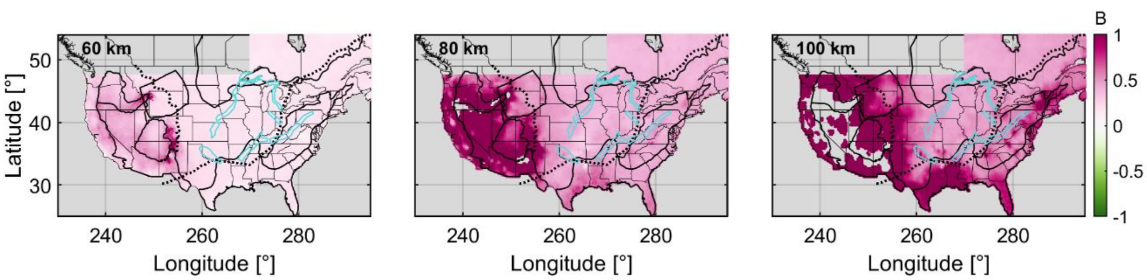

Figure 8: Calculated buoyancy number (B, eq. 6) at 60 (left), 80 (middle), and 100 km (right) depth for grid points <1300°C.

Previous work investigated convective instabilities caused by a chemically dense layer overlain by a lower viscosity fluid heated from below, equivalent to cooling a chemically buoyant cratonic root from above (Fourel et al., 2013; Jaupart et al., 2007). Jaupart et al. (2007)

found that if $0.275>B>0.5$, like shallow lithospheric values estimated above, the unstable layer can undergo oscillatory convection i.e. the alternation between cooling, densifying, and sinking of a chemically buoyant layer with reheating and rising, resulting in laterally harmonic perturbations to the interface between the layers rising and falling periodically in time (Figure 9). As noted by Jaupart *et al.* (2007) and further hypothesized by Fourel et al. (2013), these convective behaviors could explain concurrent circum- and intracratonic perturbations like rifts such as the Reelfoot Rift and basins such as the Michigan and Illinois Basins (~450 Ma, Allen and Armitage, 2012).

In young, thin lithosphere, oscillatory convection could help to prolong a shallow LAB like observed in the western United States (~60 km, Golos and Fischer, 2022; Hopper and Fischer, 2018): adiabatic asthenospheric upwellings could pass the dry peridotite solidus and keep the shallow mantle warmer through advective heat flux. These upwellings could be important to modern tholeiitic magmatism observed west of the Rocky Mountain Front. As the lithosphere thickens and upwellings do not cross the solidus, oscillatory convection could help mix shallower depleted peridotite and more fertile asthenospheric peridotite, allowing for depleted peridotite to exist at greater depths than would be predicted by adiabatic melting alone. Such mixing could potentially explain the higher Mg# in 60 km deep mantle west of the Rocky Mountain Front compared to the mantle in the cratonic portions or east of the Grenville Front, as subsolidus oscillatory convective mixing would fertilize the shallow depleted mantle. As the LAB becomes significantly deeper as seen in the cratonic mantle (>200 km, Steinberger and Becker, 2018; Yuan and Romanowicz, 2010), oscillatory convection may eventually become too slow due to increasing mantle viscosity with pressure (Hirth and Kohlstedt, 2003). This process would predict an overall decrease of cratonic mantle age with increasing depth, but also predicts the presence of some older outliers at depth due to convective mixing, as observed (Pearson, 1999).

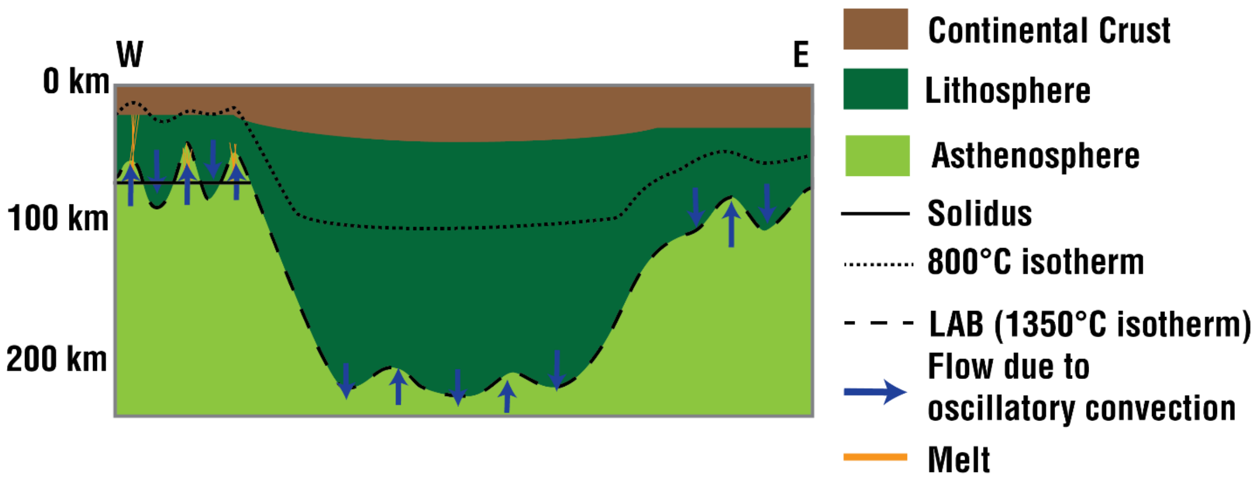

Figure 9: Schematic diagram depicting how oscillatory convection might act in the western, central, and eastern continental United States. The 800°C isotherm is schematically drawn based on our 60–100 km results and delimits where mantle would be unable to viscously flow. The solidus line depicts the depth at which melting would occur along the adiabat.

7. Conclusion

Understanding the thermomechanical state of the mantle beneath the continental United States is vital for our understanding of the current mantle flow and force balance, as density and strength control the stability and evolution of continental lithosphere. To constrain the temperature and density beneath the continental United States, we applied WISTFUL (Shinevar et al., 2022) to analyze MITPS_20 (Golos et al., 2020), a joint body and surface wave tomographic inversion for V_p and V_s variations with high resolution in the shallow mantle. Our results confirm predictions that the mantle east of the Rocky Mountains is significantly colder than that to the west. We interpret lateral temperature variations beneath the continental United States of up to 900°C, in agreement with predictions of other seismic interpretations (Afonso et al., 2016; Tesauro et al., 2014).

Our results reveal long-wavelength thermal anomalies in the east. Some are correlated with surface expressions of historic rifting events, such as the Oklahoma Aulacogen and Mid-Continent Rift, while other thermal anomalies are correlated with recent magmatism, predicted plumes, or hypothesized edge-driven convection, such as the Northern and Central Appalachian Anomalies. The highest temperatures in the west are located under Holocene volcanics and the Rio Grande Rift. The cratonic eastern United States is slightly more Fe-depleted compared to the western United States (Mg# 91 compared to Mg# 90) at 80 and 100 km. Our results generally agree within error with recent xenolith compositions and with results from xenolith thermobarometry.

Density plays a key role in the stability of cratonic mantle roots through Earth's history and our workflow provides the opportunity to explore how density predictions are controlled by temperature and composition via B value analysis. We find that our estimates of de-densification due to chemical depletion do not fully compensate for the density increase due to temperature in cratonic regions (B=0.4–0.55 at 80 and 100 km), in agreement with recent geophysical and geochemical studies (Eaton and Claire Perry, 2013; Forte et al., 1995; Kaban et al., 2003; Schutt and Lesher, 2006; Shapiro et al., 1999a). At these B values, the mantle lithosphere beneath the continental United States is within the parameter range of oscillatory convection, in which cooling, densification, and sinking of a chemically buoyant layer alternates with reheating and rising of that layer. This process could be important with respect to prolonged warming of thin lithosphere and modern magmatism in the western United States.

8. Acknowledgments

We thank Peter Molnar, Brad Hager, Daniel Lizarralde, Fiona Darbyshire, Leigh Royden, and Matej Pec for discussions. Funding was provided by NSF Grants EAR-18-44340 (MB), EAR-17-22935 (OJ), EAR-19-52642 (WS), and EAR-19-52725 (EG).

References

Afonso, J.C., Ranalli, G., Fernàndez, M., Griffin, W.L., O'Reilly, S.Y., Faul, U., 2010. On the Vp/Vs-Mg# correlation in mantle peridotites: Implications for the identification of thermal and compositional anomalies in the upper mantle. Earth Planet. Sci. Lett. 289, 606–618. https://doi.org/10.1016/j.epsl.2009.12.005

Afonso, J.C., Rawlinson, N., Yang, Y., Schutt, D.L., Jones, A.G., Fullea, J., Griffin, W.L., 2016. 3-D multiobservable probabilistic inversion for the compositional and thermal structure of the lithosphere and upper mantle: III. Thermochemical tomography in the Western-Central U.S. J. Geophys. Res. Solid Earth 121, 7337–7370. https://doi.org/10.1002/2016JB013049

Allen, P.A., Armitage, J.J., 2012. Cratonic Basins, in: Tectonics of Sedimentary Basins. John Wiley & Sons, Ltd, Chichester, UK, pp. 602–620. https://doi.org/10.1002/9781444347166.ch30

Atwater, T., 1989. Plate tectonic history of the northeast Pacific and western North America, in: The Geology of North America: The Northeastern Pacific Ocean and Hawaii. Geological Society of America.

Baptiste, V., Tommasi, A., 2014. Petrophysical constraints on the seismic properties of the Kaapvaal craton mantle root. Solid Earth 5, 45–63. https://doi.org/10.5194/se-5-45-2014

Behn, M.D., Hirth, G., Elsenbeck, J.R., 2009. Implications of grain size evolution on the seismic structure of the oceanic upper mantle. Earth Planet. Sci. Lett. 282, 178–189. https://doi.org/10.1016/j.epsl.2009.03.014

Bernardino, M. V., Jones, C.H., Levandowski, W., Bastow, I., Owens, T.J., Gilbert, H., 2019. A multicomponent isabella anomaly: Resolving the physical state of the Sierra Nevada upper mantle from Vp/Vs anisotropy tomography. Geosphere 15, 2018–2042. https://doi.org/10.1002/9781118100509.ch@

Braile, L.W., Hinze, W.J., Sexton, J.L., Keller, G.R., Lidiak, E.G., 1984. Tectonic development of the New Madrid seismic zone. US Geol. Surv. Open File Rep. 84, 204–233.

Brueseke, M.E., Hobbs, J.M., Bulen, C.L., Mertzman, S.A., Puckett, R.E., Walker, J.D., Feldman, J., 2016. Cambrian intermediate-mafic magmatism along the Laurentian margin: Evidence for flood basalt volcanism from well cuttings in the Southern Oklahoma Aulacogen (U.S.A.). Lithos 260, 164–177. https://doi.org/10.1016/j.lithos.2016.05.016

Chin, E.J., Lee, C.T.A., Luffi, P., Tice, M., 2012. Deep lithospheric thickening and refertilization beneath continental arcs: Case study of the P, T and compositional evolution of peridotite xenoliths from the Sierra Nevada, California. J. Petrol. 53, 477–511. https://doi.org/10.1093/petrology/egr069

Cipar, J.H., Garber, J.M., Kylander-Clark, A.R.C., Smye, A.J., 2020. Active crustal differentiation beneath the Rio Grande Rift. Nat. Geosci. 13, 758–763. https://doi.org/10.1038/s41561-020-0640-z

Connolly, J.A.D., 2009. The geodynamic equation of state: What and how. Geochemistry, Geophys. Geosystems 10. https://doi.org/10.1029/2009GC002540

Cox, R.T., Van Arsdale, R.B., 2002. The Mississippi Embayment, North America: A first order continental structure generated by the Cretaceous superplume mantle event. J. Geodyn. 34, 163–176. https://doi.org/10.1016/S0264-3707(02)00019-4

Currie, C.A., van Wijk, J., 2016. How craton margins are preserved: Insights from geodynamic models. J. Geodyn. 100, 144–158. https://doi.org/10.1016/j.jog.2016.03.015

Dave, R., Li, A., 2016. Destruction of the Wyoming craton: Seismic evidence and geodynamic processes. Geology 44, 883–886. https://doi.org/10.1130/G38147.1

Eaton, D.W., Claire Perry, H.K., 2013. Ephemeral isopycnicity of cratonic mantle keels. Nat. Geosci. 6, 967–970. https://doi.org/10.1038/ngeo1950

English, J.M., Johnston, S.T., 2004. The Laramide Orogeny: What Were the Driving Forces? Int. Geol. Rev. 46, 833–838. https://doi.org/10.2747/0020-6814.46.9.833

Forte, A.M., Dziewonski, A.M., Connell, R.J.O., 1995. Continent-Ocean Chemical Heterogeneity in the Mantle Based on Seismic Tomography. Science (80-.). 268, 386–389.

Fourel, L., Milelli, L., Jaupart, C., Limare, A., 2013. Generation of continental rifts , basins , and swells by lithosphere instabilities 118, 3080–3100. https://doi.org/10.1002/jgrb.50218

Goes, S., van der Lee, S., 2002. Thermal structure of the North American uppermost mantle inferred from seismic tomography. J. Geophys. Res. 107. https://doi.org/10.1029/2000jb000049

Golos, E.M., Fang, H., van der Hilst, R.D., 2020. Variations in Seismic Wave Speed and VP/VS Ratio in the North American Lithosphere. J. Geophys. Res. Solid Earth 125. https://doi.org/10.1029/2020JB020574

Golos, E.M., Fischer, K.M., 2022. New Insights Into Lithospheric Structure and Melting Beneath the Colorado Plateau. Geochemistry, Geophys. Geosystems 23. https://doi.org/10.1029/2021gc010252

Hatcher, R.D., 2010. The Appalachian orogen: A brief summary. Mem. Geol. Soc. Am. 206, 1–19. https://doi.org/10.1130/2010.1206(01)

Hirth, G., Kohlstedt, D.L., 2003. Rheology of the Upper Mantle and the Mantle Wedge : A View from the Experimentalists upper mantle . We first analyze experimental data to provide a critical review of flow. Geophys. Monogr. Ser. 138, 83–105. https://doi.org/10.1029/138GM06

Holland, T.J.B., Green, E.C.R., Powell, R., 2018. Melting of peridotites through to granites: A simple thermodynamic model in the system KNCFMASHTOCr. J. Petrol. 59, 881–900. https://doi.org/10.1093/petrology/egy048

Holland, T.J.B., Powell, R., 2011. An improved and extended internally consistent thermodynamic dataset for phases of petrological interest, involving a new equation of state for solids. J. Metamorph. Geol. 29, 333–383. https://doi.org/10.1111/j.1525-1314.2010.00923.x

Hopper, E., Fischer, K.M., 2018. The Changing Face of the Lithosphere-Asthenosphere Boundary: Imaging Continental Scale Patterns in Upper Mantle Structure Across the Contiguous U.S. With Sp Converted Waves. Geochemistry, Geophys. Geosystems 19, 2593–2614. https://doi.org/10.1029/2018GC007476

Jaupart, C., Molnar, P., Cottrell, E., 2007. Instability of a chemically dense layer heated from below and overlain by a deep less viscous fluid, Journal of Fluid Mechanics. https://doi.org/10.1017/S0022112006003521

Jordan, T.H., 1975. The continental tectosphere. Rev. Geophys. 13, 1. https://doi.org/10.1029/RG013i003p00001

Kaban, M.K., Schwintzer, P., Artemieva, I.M., Mooney, W.D., 2003. Density of the continental roots: Compositional and thermal contributions. Earth Planet. Sci. Lett. 209, 53–69. https://doi.org/10.1016/S0012-821X(03)00072-4

Kane, M.F., Godson, R.H., 1989. A crust/mantle structural framework of the conterminous United States based on gravity and magnetic trends. pp. 383–404. https://doi.org/10.1130/MEM172-p383

Kelly, R.K., Kelemen, P.B., Jull, M., 2003. Buoyancy of the continental upper mantle.

Geochemistry, Geophys. Geosystems 4. https://doi.org/10.1029/2002GC000399

Kennett, B.L.N., Engdah, E.R., Buland, R., 1995. Constraints on seismic velocities in the Earth from traveltimes 108–124.

Khan, A., Zunino, A., Deschamps, F., 2011. The thermo-chemical and physical structure beneath the North American continent from Bayesian inversion of surface-wave phase velocities. J. Geophys. Res. Solid Earth 116, 1–23. https://doi.org/10.1029/2011JB008380

Krauss, Z., Menke, W., 2020. The Northern Gulf Anomaly: P- and S-wave travel time delays illuminate a strong thermal feature beneath the Northern Gulf of Mexico. Earth Planet. Sci. Lett. 534, 116102. https://doi.org/10.1016/j.epsl.2020.116102

Kreemer, C., Blewitt, G., Klein, E.C., 2014. A geodetic plate motion and Global Strain Rate Model. Geochemistry, Geophys. Geosystems 15, 3849–3889. https://doi.org/10.1002/2014GC005407

Lee, C.-T.A., 2003. Compositional variation of density and seismic velocities in natural peridotites at STP conditions: Implications for seismic imaging of compositional heterogeneities in the upper mantle. J. Geophys. Res. Solid Earth 108. https://doi.org/10.1029/2003jb002413

Leeman, W.P., 1982. Development of the Snake River Plain-Yellowstone Plateau Province : an overview and petrologic model, in: Cenozoic Geology of Idaho. pp. 155–177.

Levandowski, W., Jones, C.H., Shen, W., Ritzwoller, M.H., Schulte-Pelkum, V., 2014. Origins of topography in the western U.S.: Mapping crustal and upper mantle density variations using a uniform seismic velocity model. J. Geophys. Res. Solid Earth 119, 2375–2396. https://doi.org/10.1002/2013JB010607

Lévěque, J.-J., Rivera, L., Wittlinger, G., 1993. On the use of the checker-board test to assess the resolution of tomographic inversions. Geophys. J. Int. 115, 313–318. https://doi.org/10.1111/j.1365-246X.1993.tb05605.x

Levin, V., Long, M.D., Skryzalin, P., Li, Y., López, I., 2018. Seismic evidence for a recently formed mantle upwelling beneath New England. Geology 46, 87–90. https://doi.org/10.1130/G39641.1

Li, Z.X.A., Lee, C.T.A., Peslier, A.H., Lenardic, A., Mackwell, S.J., 2008. Water contents in mantle xenoliths from the Colorado Plateau and vicinity: Implications for the mantle rheology and hydration-induced thinning of continental lithosphere. J. Geophys. Res. Solid Earth 113. https://doi.org/10.1029/2007JB005540

Mareschal, J.C., Jaupart, C., 2013. Radiogenic heat production, thermal regime and evolution of continental crust. Tectonophysics 609, 524–534. https://doi.org/10.1016/j.tecto.2012.12.001

Marzoli, A., Callegaro, S., Dal Corso, J., Davies, J.H.F.L., Chiaradia, M., Youbi, N., Bertrand, H., Reisberg, L., Merle, R., Jourdan, F., 2018. The Central Atlantic Magmatic Province (CAMP): A Review. https://doi.org/10.1007/978-3-319-68009-5_4

Mazza, S.E., Gazel, E., Johnson, E.A., Kunk, M.J., McAleer, R., Spotila, J.A., Bizimis, M., Coleman, E.S., 2014. Volcanoes of the passive margin: The youngest magmatic event in eastern North America. Geology 42, 483–486. https://doi.org/10.1130/G35407.1

Menke, W., Skryzalin, P., Levin, V., Harper, T., Darbyshire, F., Dong, T., 2016. The Northern Appalachian Anomaly: A modern asthenospheric upwelling. Geophys. Res. Lett. 43, 10,173-10,179. https://doi.org/10.1002/2016GL070918

Molnar, P., England, P.C., Jones, C.H., 2015. Mantle dynamics, isostasy, and the support of high terrain. J. Geophys. Res. Solid Earth 120, 1932–1957. https://doi.org/10.1002/2014JB011724

Mustelier, E.C., Menke, W., 2021. Seismic anomalies in the southeastern North American asthenosphere as characterized with body wave travel times from high-quality teleseisms. Tectonophysics 809, 228853. https://doi.org/10.1016/j.tecto.2021.228853

Parsons, T., 2006. The Basin and Range Province.

Pearson, D.G., 1999. The age of continental roots. Lithos. https://doi.org/10.1016/S0024-4937(99)00026-2

Perry, H.K.C., Forte, A.M., Eaton, D.W.S., 2003. Upper-mantle thermochemical structure below North America from seismic-geodynamic flow models. Geophys. J. Int. 154, 279–299. https://doi.org/10.1046/j.1365-246X.2003.01961.x

Petersen, M.D., Shumway, A.M., Powers, P.M., Mueller, C.S., Moschetti, M.P., Frankel, A.D., Rezaeian, S., McNamara, D.E., Luco, N., Boyd, O.S., Rukstales, K.S., Jaiswal, K.S., Thompson, E.M., Hoover, S.M., Clayton, B.S., Field, E.H., Zeng, Y., 2020. The 2018 update of the US National Seismic Hazard Model: Overview of model and implications. Earthq. Spectra 36, 5–41. https://doi.org/10.1177/8755293019878199

Schmandt, B., Humphreys, E., 2011. Seismically imaged relict slab from the 55 Ma Siletzia accretion to the northwest United States. Geology 39, 175–178. https://doi.org/10.1130/G31558.1

Schmandt, B., Lin, F., Karlstrom, K.E., 2015. Distinct crustal isostasy trends east and west of the Rocky Mountain Front. Geophys. Res. Lett. 42. https://doi.org/10.1002/2015GL066593

Schutt, D.L., Lesher, C.E., 2006. Effects of melt depletion on the density and seismic velocity of garnet and spinel lherzolite. J. Geophys. Res. Solid Earth 111, 1–24. https://doi.org/10.1029/2003JB002950

Schutt, D.L., Lowry, A.R., Buehler, J.S., 2018. Moho temperature and mobility of lower crust in the western United States. Geology 46, 219–222. https://doi.org/10.1130/G39507.1

Shapiro, S.S., Hager, B.H., Jordan, T.H., 1999a. The continental tectosphere and Earth's long-wavelength gravity field. Dev. Geotecton. 24, 135–152. https://doi.org/10.1016/S0419-0254(99)80009-3

Shapiro, S.S., Hager, B.H., Jordan, T.H., 1999b. Stability and dynamics of the continental tectosphere. Dev. Geotecton. 24, 115–133. https://doi.org/10.1016/S0419-0254(99)80008-1

Shinevar, W.J., Jagoutz, O., Behn, M.D., 2022. WISTFUL: Whole-Rock Interpretative Seismic Toolbox for Ultramafic Lithologies. Geochemistry Geophys. Geosystems 23. https://doi.org/10.1029/2022GC010329

Steinberger, B., Becker, T.W., 2018. A comparison of lithospheric thickness models. Tectonophysics 746, 325–338. https://doi.org/10.1016/j.tecto.2016.08.001

Tesauro, M., Kaban, M.K., Mooney, W.D., Cloetingh, S.A.P.L., 2014. Density, temperature, and composition of the North American lithosphere-New insights from a joint analysis of seismic, gravity, and mineral physics data: 2. Thermal and compositional model of the upper mantle. Geochemistry, Geophys. Geosystems 15, 4808–4830. https://doi.org/10.1002/2014GC005484

Venzke, E. (ed), 2013. Global Volcanism Program, 2013. Volcanoes of the World, v. 4.10.0. https://doi.org/https://doi.org/10.5479/si.GVP.VOTW4-2013

Wang, Y., Forsyth, D.W., Rau, C.J., Carriero, N., Schmandt, B., Gaherty, J.B., Savage, B., 2013. Fossil slabs attached to unsubducted fragments of the Farallon plate. Proc. Natl. Acad. Sci. U. S. A. 110, 5342–5346. https://doi.org/10.1073/pnas.1214880110

Whitmeyer, S.J., Karlstrom, K.E., 2007. Tectonic model for the Proterozoic growth of North America. Geosphere 3, 220–259. https://doi.org/10.1130/GES00055.1

Wooley, A., 1987. Alkaline rocks and carbonatites of the world, part 1: North and South America. University of Texas Press.
Workman, R.K., Hart, S.R., 2005. Major and trace element composition of the depleted MORB mantle (DMM). Earth Planet. Sci. Lett. 231, 53–72. https://doi.org/10.1016/j.epsl.2004.12.005
Yang, X., Gao, H., 2018. Full-Wave Seismic Tomography in the Northeastern United States: New Insights Into the Uplift Mechanism of the Adirondack Mountains. Geophys. Res. Lett. 45, 5992–6000. https://doi.org/10.1029/2018GL078438
Yuan, H., Romanowicz, B., 2010. Lithospheric layering in the North American craton. Nature 466, 1063–1068. https://doi.org/10.1038/nature09332
Zandt, G., Gilbert, H., Owens, T.J., Ducea, M., Saleeby, J., Jones, C.H., 2004. Active foundering of a continental arc root beneath the southern Sierra Nevada in California. Nature 431, 41–46. https://doi.org/10.1038/nature02847
Zoback, M. Lou, Mooney, W.D., 2003. Lithospheric buoyancy and continental intraplate stresses. Int. Geol. Rev. 45, 95–118. https://doi.org/10.2747/0020-6814.45.2.95